University of Oklahoma

Graduate College

Modeling Optical and Photochemical Properties of Biomedical Imaging Dyes

A Dissertation

Submitted to the Graduate Faculty

in partial fulfillment of the requirements for the

Degree of

Doctor of Philosophy

By: Carly Wickizer

Norman, Oklahoma

2026

Modeling Optical and Photochemical Properties
of Biomedical Imaging Dyes

A dissertation approved for the
Department of Chemistry and Biochemistry

By the committee consisting of

Dr. Wai Tak Yip, Chair

Dr. Yihan Shao

Dr. Bayram Saparov

Dr. Yitong Dong

Dr. Madalina Furis

Contents

List of Figures

List of Tables

List of Acronyms and Abbreviations

AD Alzheimer's disease.

AO Atomic Orbital.

BL Bioluminescence.

CI Conical Intersection.

CIEEL Chemically initiated electron exchange luminescence.

CL Chemiluminescence.

CT Charge-Transfer.

CTID Charge-transfer induced decomposition.

CTIL Charge-transfer induced luminescence.

CTZ Coelenterazine.

DFT Density Functional Theory.

DMSO Dimethyl sulfoxide.

DTZ Diphenylterazine.

EDG Electron Donating Group.

ETM Ethyltrimethylammonium.

FDO Firefly Dioxetanone.

FL Fluorescence.

FLI Fluorescence Imaging.

FSM Freezing String Methid.

HOMO Highest Occupied Molecular Orbital.

IPO Imidazopyrazinone.

IRC Intrinsic Reaction Coordinate.

KS Kohn-Sham.

LUMO Lowest Occupied Molecular Orbital.

MECP Minumum Energy Crossing Point.

MEP Minumum Energy Path.

MO Molecular Orbital.

MR Mixed-Reference.

MRI Magnetic Resonance Imaging.

MRSF-TDDFT Mixed-Reference Spin-Flip Time-Dependent Density Functional Theory.

MSOT Multispectral Optoacoustic Tomography.

NAMD Non-adiabatic Molecular Dynamics.

NIR Near-infrared.

NIRF Near-infrared Fluorescence.

OA Optoacoustic.

OAI Optoacoustic Imaging.

OAT Optoacoustic Tomography.

OI Optical Imaging.

PA Photoacoustic.

PBE Perdew-Burke-Ernzerhof.

PBS Phosphate Buffered Saline.

QY Quantum Yield.

RDM Reduced Density Matrices.

SET Single Electron Transfer.

SF Spin-Flip.

SF-TDDFT Spin-Flip Time-Dependent Density Functional Theory.

SNR Signal-to-Noise Ratio.

TDDFT Time-Dependent Density Functional Theory.

TDKS Time-Dependent Kohn-Sham.

TDM Transition Dipole Moment.

TS Transition State.

XC Exchange-correlation.

Acknowledgements

I am immensely grateful to have had the mentorship of Dr. Yihan Shao throughout my doctoral research. Aside from the knowledge of computational chemistry and electronic structure theory that he has imparted to me, his enthusiastic and inquisitive nature has shaped the manner in which I approach all scientific endeavors. Prior to 2021, I had no experience with computational chemistry, much less Python or even command line. My success would not have been possible without the help of my fellow CCATS, who never lost patience helping me overcome this learning curve.

I would also like to express gratitude for the support of my committee members: Dr. Bayram Saparov, Dr. Yitong Dong, Dr. Madalina Furis, and especially Dr. Wai Tak Yip for taking on the role of committee chair during this final semester. In addition, I am extremely thankful to have had the opportunity to work with experimental collaborators Dr. Lacey McNally on squaraine dyes, and Dr. Chongzhao Ran on ADLumin dyes.

The encouragement from my parents, family, and friends has meant the world to me throughout this journey. Their love and support has been a constant reminder of what matters most. Lastly, I want to thank Chance Lander. While I am proud of the work we have accomplished, I consider the partnership we've built to be my greatest success. Thank you for your mentorship and for being the most invaluable part of this experience.

Abstract

This dissertation focuses on modeling optical and photochemical properties of biomedical imaging dyes. Specifically, two optical imaging systems are examined: optoacoustic and chemiluminescent dyes. The first chapter provides motivation and background information for these particular modalities, as well as a brief discussion of the computational approaches employed.

The second chapter presents a computational study of squaraine dyes to facilitate an understanding of how structural features influence optoacoustic signal generation. The specific foci of this investigation are two features most relevant to optoacoustic signal generation: absorption and non-radiative relaxation. This work highlights how minor substituent modifications have a substantial impact on absorption properties and explain these effects via analysis of frontier molecular orbitals (MOs). In addition, the role of structural flexibility is examined and a path for further work in this area is described.

The last two chapters focus on separate processes contributing to chemiluminescence in imidazopyrazinone dyes. The third chapter presents a computational modeling of ground state reactions that precede chemiexcitation, namely how different substituents affect the formation of a necessary dioxetanone intermediate. The fourth and final chapter focuses on the dioxetanone decomposition that produces the final excited state intermediate, as well as the emission wavelength of this product. Here we examine the relationship between substituent groups and frontier MO energies and present preliminary results for modeling the S_0/S_1 conical intersection. This work demonstrates the interplay between multiple aspects of probe development, with a key insight into how modifications that produce desired emission wavelengths may result in higher energy barriers for chemiluminescent activation.

Chapter 1

Introduction

1.1 Motivations for Computational Studies of Optical Imaging Dyes

In vivo medical imaging is essential for diagnosis and treatment, and the development of better contrast agents has been an ongoing effort for many years.[6] More recently, there has been a focus on combining structural and functional imaging to provide a more robust visualization of molecular-level processes.[1,7–9] The concept of hybrid imaging is depicted in Fig.1.1; it is important to note that structural techniques like MRI and CT can be supplemented by contrast agents to yield functional information as well. A major advantage of this concept is the possibility for the development of more accessible technologies without the drawbacks of ionizing radiation or cost/time inefficiency. Optical imaging (OI) methods such as fluorescence or bio/chemiluminescence can be supplemented with ultrasound (US). In addition, optoacoustic tomography (OAT) has developed in recent years as a standalone OI modality that inherently provides functional information.

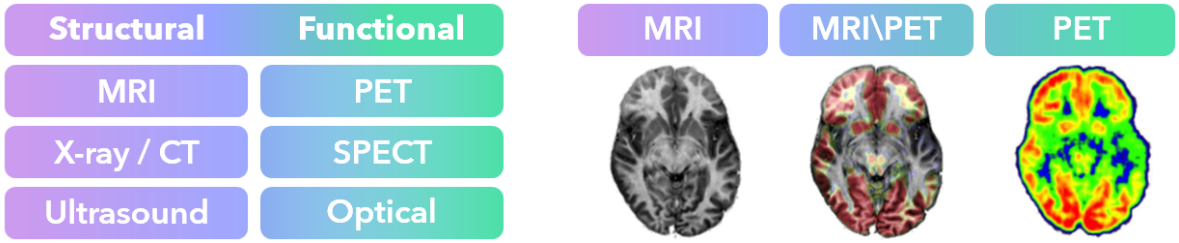

Figure 1.1: The classification of imaging techniques as structural or functional, which are combined in hybrid modalities such as MRI/PET. Adapted from ref 1.

Clinical applications of OI have been limited by penetration depth, an issue which arises from the interactions of photons with tissue (Fig. 1.2). This can be mitigated, though not completely eliminated, by the use of chromophores that are active in the more bio-transparent near infrared (NIR) region. In addition to penetration depth, it can be difficult to distinguish excitation light or scattering from signal emitted by the target, which decreases the signal to noise ratio (SNR). Due to these factors, OI methods that rely on a one-way photon path (opposed to the two-way path shown in Fig.1.2) are more promising for clinical translation. As such, the work presented here will focus on the development of probes for optoacoustic (OA) and chemiluminescence (CL) imaging.

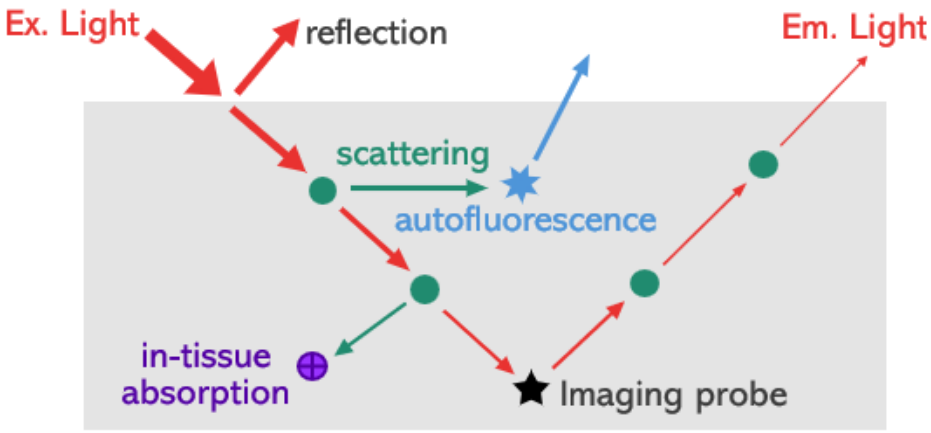

Figure 1.2: Schematic representation of the path of a photon beam in tissue demonstrating various mechanisms by which fluorescence signal is decreased.

1.2 Fundamentals of Optoacoustic Imaging

The photoacoustic (PA) effect was first documented by Alexander Graham Bell in his 1880 paper, "On the production and reproduction of sound by light".[10] The more general term "radiophony" was adapted after the realization that the phenomenon resulted from all forms of electromagnetic radiation.[11] Today, "photoacoustic" – used synonymously with "optoacoustic" – specifies optical light as the radiant energy source. The PA effect was first applied

to biomedical imaging in 1964 using pulsed laser excitation, which relies on the thermoelastic mechanism.[11] In this process, pulsed excitations cause local heating and elastic expansion of the surrounding medium, which generates pressure waves (Fig. 1.3). Ultrasound detection of these pressure waves allows for a greater tissue penetration depth and SNR compared to photon emission. The magnitude of the initial pressure rise is given by:[12]

$$p_0 = \mathbf{\Phi}(\boldsymbol{x}, \lambda)\mu_a(\lambda)\Gamma_{eff} \tag{1.1}$$

Where $\mathbf{\Phi}(\boldsymbol{x}, \lambda)$ is the fluence of light with wavelength λ at position $\boldsymbol{x}$, $\mu_a(\lambda)$ is the optical absorption coefficient of the chromophore at wavelength λ, and the thermoelastic conversion efficiency is given by $\Gamma_{eff} = \Gamma(1 - QY)$, where QY is the fluorescent quantum yield and Γ is the dimensionless Grüneisen parameter that describes thermodynamic properties of the propagating medium.

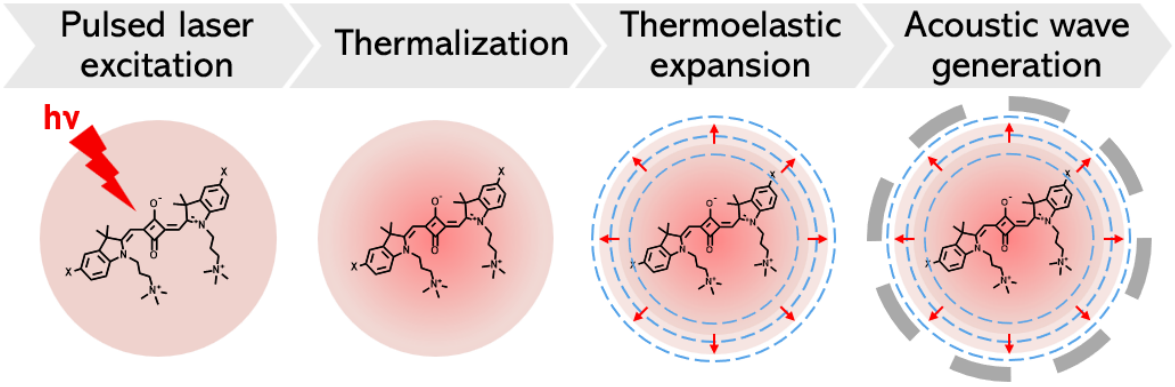

Figure 1.3: The photoacoustic effect in the context of optoacoustic imaging (OAI).

From Eq. 1.1, two important characteristics for OA probes can be deduced: high optical absorption coefficient ($\mu_a(\lambda)$) and low fluorescent quantum yield (QY). In the context of developing probes for use in biomedical imaging, we also know that absorption in the NIR region is optimal for tissue penetration as there are less interactions with endogenous chromophores. In addition, it is reasonable to assume that all non-radiative relaxation will occur

through vibrations. Thus, our computational efforts should be directed towards understanding how structural features influence: i) absorption strength, ii) absorption wavelength, and iii) the rate of vibrational relaxation.

1.3 Fundamentals of Chemiluminescence Imaging

Chemiluminescence (CL) and bioluminescence (BL) have been of interest as "molecularly generated light" sources since the discovery of luminol in 1928.[13–15] CL molecules undergo a chemical reaction to reach their electronic excited state (chemi-excitation) and emit a photon upon relaxation to the electronic ground state (Fig. 1.4). While the "round-trip" of photons in fluorescence imaging (Fig. 1.2) results in low signal-to-noise ratios (SNR) typically on the order of <5, CL imaging avoids issues caused by excitation light, such as surface reflection and autofluorescence, and can reach much higher SNR >100.[14] Most chemiexcitation reactions involve the decomposition of a cyclic peroxide.[16] One such group of CL molecules are the 1,2-dioxetanes discovered by Schaap's group,[17–20] which have been adapted into triggerable probes for a variety of analytes and are currently commercially available for in vitro assays.[21] More recent studies have demonstrated in vivo imaging of small animals,[4,5,22–24] though continued development of highly emissive probes is needed to achieve *in vivo* imaging at the human scale.

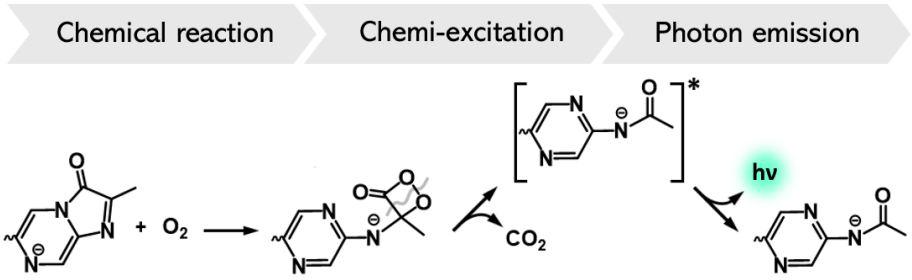

Figure 1.4: A general mechanism of chemiluminescence demonstrated for imidazopyrazinone (IPO).

Chemiluminescence is a multi-step process that involves i) a chemical trigger, ii) the generation of an chemiexcited intermediate through surface crossing of the ground and excited states (i.e., a conical intersection (CI)), and iii) photon emission by the excited state intermediate. As in the case of IPO-based CL molecules, there are sometimes multiple reaction steps between the initial chemical trigger (O_2 in Fig. 1.4) and the chemiexcited intermediate. Each of these processes can be modeled, leading to insights into where bottlenecks may exist and how they may be mitigated through structural modifications. In addition, as emission in the NIR wavelength range is desirable for *in vivo* CL probes, further modifications can be suggested and examined for their effects on CL efficiency.

1.4 Review of Computational Methods Applied to Optoacoustic and Chemiluminescence Imaging

Density functional theory (DFT) has been widely applied in the theoretical study of photophysical processes, yielding qualitatively accurate results with low computational cost. Within ground state DFT, the molecular orbitals $\psi_{k\sigma}$ are eigenfunctions of the Kohn-Sham (KS) eigenvalue problem:

$$\hat{F}_\sigma \psi_{k\sigma}(\mathbf{r}) = \varepsilon_k \psi_{k\sigma}(\mathbf{r}) \tag{1.2}$$

where the Fock operator contains external (v_{ext}) and Hartree (v_{H}) potentials, as well as the exchange-correlation (XC) potential ($\hat{v}^\sigma_{\text{xc}}$) determined by the choice of functional. $\psi_{k\sigma}(\mathbf{r})$ are the Kohn-Sham molecular orbitals (MOs).

$$\hat{F}_\sigma = -\frac{1}{2}\hat{\nabla}^2 + v_{\text{ext}} + v_{\text{H}} + \hat{v}^\sigma_{\text{xc}} \tag{1.3}$$

DFT can be extended to the study of excited states via the time-dependent Kohn-Sham (TDKS) equation:

$$i\hbar\frac{d}{dt}\psi_{k\sigma}(\mathbf{r},t) = \hat{F}_\sigma\psi_{k\sigma}(\mathbf{r},t) \tag{1.4}$$

Starting from this equation, one can derive the linear response formalism, which is commonly referred to as time-dependent density functional theory (TDDFT), for computing excitation energies (ω) and amplitudes ($\mathbf{X}$ and $\mathbf{Y}$) through the Casida equation:

$$\begin{pmatrix} \mathbf{A} & \mathbf{B} \\ \mathbf{B}^* & \mathbf{A}^* \end{pmatrix}\begin{pmatrix} \mathbf{X} \\ \mathbf{Y} \end{pmatrix} = \omega\begin{pmatrix} 1 & 0 \\ 0 & -1 \end{pmatrix}\begin{pmatrix} \mathbf{X} \\ \mathbf{Y} \end{pmatrix} \tag{1.5}$$

where elements of the $\mathbf{A}$ and $\mathbf{B}$ matrices are given by:

$$A_{ia,jb} = \delta_{ij}\delta_{ab}(\varepsilon_a - \varepsilon_i) + \langle ia|jb\rangle - C_{\mathrm{HF}}\langle ij|ab\rangle + \langle ia|f_{xc}|jb\rangle \tag{1.6}$$

$$B_{ia,jb} = \langle ia|bj\rangle - C_{\mathrm{HF}}\langle ib|aj\rangle + \langle ia|f_{xc}|bj\rangle \tag{1.7}$$

using indices *i, j* and *a, b* for occupied and virtual MOs. Whereas the DFT ground state is variationally optimized via Eq. 1.2, the TDDFT excited states obtained from Eq. 1.5 are variational with respect to each other, but not to the ground state.[25] While TDDFT yields semi-quantitative results for vertical excitation energies, inaccuracies arise in regions where the ground and excited states are nearly degenerate.

Most importantly, conical intersections (CIs) are degeneracies between electronic states, and are critical in photochemistry as they facilitate non-adiabatic transitions. A commonly used alternative method for the study of CIs is the spin-flip (SF) TDDFT method from Krylov and coworkers,[26] in which a reference state of a higher multiplicity is used to allow for a more balanced treatment of the states of interest. Within SF-TDDFT, single $\alpha \rightarrow \beta$

operations produce a set of excited state determinants that are variational.[25] The SF excited state configurations generated by a triplet $M_S = +1$ reference state are shown in blue and black in Fig. 1.5. These include what would usually be the S_0 and S_1 states, as well as a doubly excited configuration which couples the two and cannot be generated by single excitations within normal TDDFT. Shown in red are additional configurations that would be generated with $\beta \rightarrow \alpha$ spin-flip excitations from the $M_S = -1$ reference state; the absence of those configurations from the original implementation of SF-TDDFT could lead to severe spin contamination of some SF-TDDFT states.

In mixed-reference (MR) SF-TDDFT from Choi and coworkers, the reduced density matrices (RDM) of the $M_S = +1$ and $M_S = -1$ reference states are combined into a mixed-reference RDM (MR-RDM),[27] which is then used to generate spin-flipped electronic configurations, including those red configurations in 1.5 missing from the original SF-TDDFT model. While the configurations shown in gray in Fig. 1.5 are still not included, they contribute only to higher energy states and expected not to make a significant contribution to the excitation amplitudes ($\mathbf{X}$) and energies (ω) of the low-lying excited states of interest in biomedical imaging.

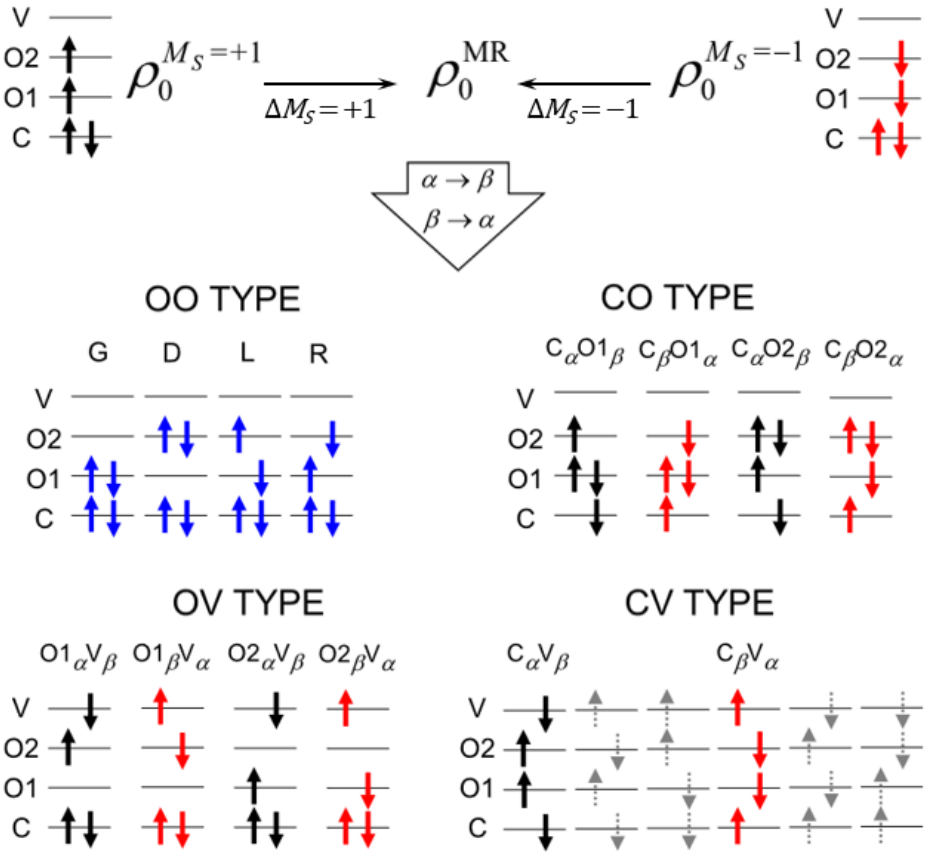

Figure 1.5: Upper panel: An example of two 4-electron triplet reference states used in MRSF-TDDFT. Lower panel: Electronic configurations generated in SF (blue, black) and MRSF (blue, black, red). Configurations not considered by MRSF are in gray. Adapted from ref 2.

Chapter 2

Effect of Structural Modifications on Optoacoustic Imaging Probes

2.1 Introduction

Optoacoustic imaging (OAI) combines molecular-level visualization enabled by optical contrast with the penetration depth offered by ultrasound detection. Studies in humans have already demonstrated success in resolving endogenous chromophores, as well as FDA-approved fluorescent dyes and labels.[28] As discussed in Chapter 1.2, optoacoustic OA signal generation relies on the generation of thermal energy via non-radiative relaxation – thus, fluorescent agents optimized for high rates of radiative relaxation are the least optimal chromophores for OAI.[29] However, until the relatively recent rise in interest for OAI as a clinical imaging modality, there has never been a need for FDA approved chromophores that do not emit light.

Towards the goal of developing exogenous contrast agents optimized for OAI, this chapter focuses on structure-function relationships that define OA signal generation ability: strong absorbance and non-radiative relaxation. The effects of structural modifications on absorbance and absorption wavelength were examined through TDDFT excitation spectra and frontier molecular orbital analysis. While non-radiative relaxation was not studied directly in this work, vibrational motions that may facilitate relaxation were quantified via DFT vibrational entropy calculations.

2.2 Background: Previous Experimental Work

Squaraine dyes are characterized by an electron-deficient squaric acid core which can be functionalized symmetrically or unsymmetrically with electron-donating groups. This tunability has yielded a wide variety of applications in chromophore design.[30,31] Of particular interest to the field of OA probe development is the simplicity of the core four-membered ring, which offers a unique opportunity to study the relationship between structure and signal generation. With this motivation, collaborators synthesized a set of squaraine dyes as shown in Fig 2.1. The side chains were modified symmetrically at the X-position with atoms of varying weight and electronegativy. In addition, flexibility was introduced by replacing the CH_3 R-group with ethyltrimethylammonium (ETM). Here, the analogs will be referred to by their X and R substituents: i.e., Br-ETM indicates the squaraine with X = Br and R = ETM.

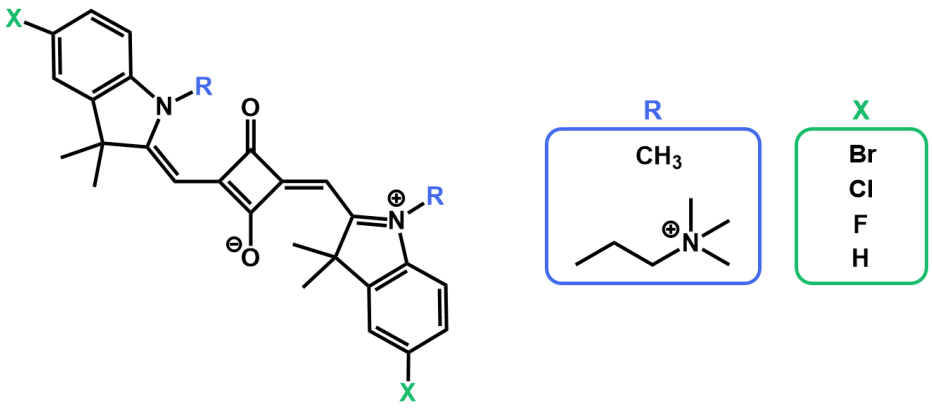

Figure 2.1: Structures of squaraine analogs, where X= Br, Cl, F, or H and R= CH_3 or ETM.

OA signal generated by a chromophore is dependent on the absorption profile, as well as the ability to generate thermal energy through non-radiative relaxation.[12,32] Shown in Fig. 2.2 are experimentally measured Multispectral Optoacoustic Tomography (MSOT) and absorption spectra for the six squaraine analogs. The MSOT spectrum can be thought of as

the ultrasound signal detected at each excitation wavelength, which ranges from 680 to 780 nm for this particular instrument. Interestingly, the absorption spectra showed no distinguishable activity in this region (inset of Fig. 2.2b). Thus, our computational investigation focused on two questions:

- Why is MSOT signal clearly detectable when no excitation is observed?
- What causes the trend in MSOT signal intensity?

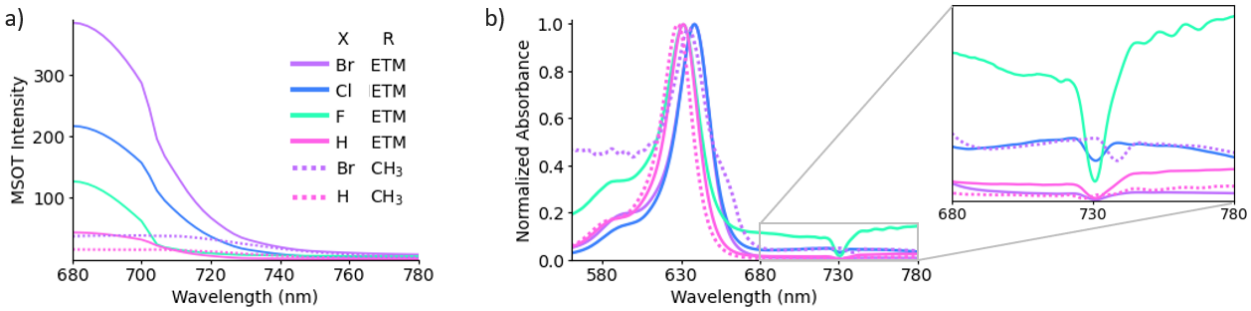

Figure 2.2: Experimental results adapted from ref 3. a) MSOT spectra of squaraine analogs in tissue-mimicking phantoms. b) Normalized absorption spectra of squaraine analogs in buffer solution, where the inset shows the MSOT excitation wavelength region (680-780nm).

2.3 Methods

Ground-state geometry optimizations and TDDFT calculations were performed in gas phase using the PBE functional[33] and 6-31+G* basis set.[34] All calculations were carried out using the Q-Chem 5.4 software package.[35] After determining the lowest energy conformations, TDDFT excitation energies and oscillator strengths were calculated at the optimized ground state geometries. In order to obtain vibrational entropies, frequency calculations were also done at the optimized ground state geometries. Absorption spectra were plotted as:

$$f(\lambda) = \sum_k f_k(\lambda) = \sum_k f_k \exp\left(\frac{-(\lambda - \lambda_k)^2}{\sigma^2}\right) \tag{2.1}$$

where λ_k and f_k are the k-th excitation wavelengths and oscillator strengths from TDDFT calculations, and a broadening factor (σ) of 15 nm was used. Eq. 2.1 broadens the calculated stick spectra in order to provide a more realistic absorption profile, but does not effect the height of peaks relative to one another.

2.4 Absorption Spectra of Squaraine Dyes

Calculated absorption spectra for the squaraine analogs are shown in Fig. 2.3, where the inset displays the region from 680-780 nm. The most prominent excitations (S_2) are in the 580-630 nm range, which aligns well with the experimentally measured spectra in Fig. 2.2b. In addition, all molecules were calculated to have a small peak around 700 nm (S_1), which was not distinguishable in the experimental spectra, likely due to the relatively low intensity. As S_1 is the only excitation found within the MSOT wavelength range, it was determined to be responsible for the MSOT signal generated by the squaraine dyes (Fig. 2.2a) and is the focus of further analysis. Analogous to absorbance, the computational oscillator strength is given by:

$$f_k = \frac{2}{3}\Delta E_k |\vec{\mu}_k|^2 \tag{2.2}$$

where $\vec{\mu}_k$ is the transition dipole moment for the excitation with an energy of $\Delta E_k = \hbar\omega_k = h\frac{C}{\lambda_k}$. The calculated oscillator strengths for the S_1 excitations correlate well with the trend in observed MSOT intensities, increasing with the weight of the atom at the X-position, and overall much weaker for the R = CH_3 analogs. These results are tabulated in Table A.1.

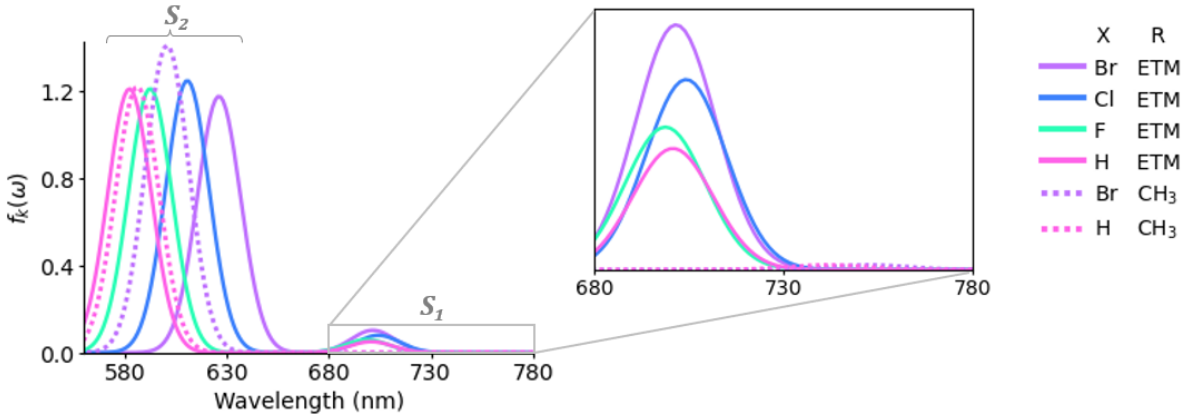

Figure 2.3: Absorption spectra of squaraine analogs calculated using the PBE functional and 6-31+G* basis set. The inset shows the MSOT excitation wavelength region (680-780nm). S_1 and S_2 indicate the first and second singlet excited states, respectively. Adapted from ref 3.

In order to explain the effect of substituents on transition dipole moment, one can examine the character of the molecular orbital (MO) transitions contributing to the excitation. Specifically, the transition dipole moment ($\vec{\mu}_k$) couples the initial (Ψ_0) and final (Ψ_k) wavefunctions through the electric dipole moment operator ($\hat{\mu}$)

$$\vec{\mu}_k = \langle \Psi_k | \hat{\mu} | \Psi_0 \rangle = \sum_{ai} \left(X_{ai}^k + Y_{ai}^k \right) \langle \psi_a | \hat{\mu} | \psi_i \rangle \tag{2.3}$$

where X_{ai}^k and Y_{ai}^k are excitation and de-excitation amplitudes between the i-th occupied MO and the a-th unoccupied orbital (Eq. 1.5). For low-lying excited states, such as S_1, the amplitudes (X_{ai} and Y_{ai}) are significant only for frontier orbitals, such as the highest occupied molecular orbital (HOMO), the second highest occupied molecular orbital (HOMO-1), and the lowest unoccupied orbital (LUMO). Therefore, two key factors that influence the magnitude of $\vec{\mu}_k$ are the spatial distribution and overlap of these frontier MOs.

The HOMO-1, HOMO, and LUMO for all squaraine analogs are shown in Fig. 2.4, where the values on the blue and red arrows indicate the HOMO→LUMO and HOMO-1→LUMO transition amplitudes for S_1. In general, the HOMO and LUMO are delocalized over nearly the entire molecule, while the HOMO-1 is much more localized on the center. The HOMO-1→LUMO transition is thus partially of charge-transfer (CT) character due to the low spatial overlap of the two MOs, which decreases the transition dipole moment (TDM).[36,37] The effect of this can be seen in the variation of oscillator strength of the R=ETM analogs: as the X-group becomes lighter, the oscillator strength gets lowered due to an increase in the HOMO-1→LUMO amplitude and a decrease in the HOMO→LUMO amplitude (Fig. 2.4a). Continuing this trend, the HOMO-1→LUMO transition nearly completely dominates the ∼750 nm S_1 excitation calculated for the R=CH_3 analogs (Figs. 2.3 and 2.4b), which have the lowest oscillator strength. As such, the ETM side chain has the dual effect of increasing the oscillator strength, while decreasing the excitation wavelength.

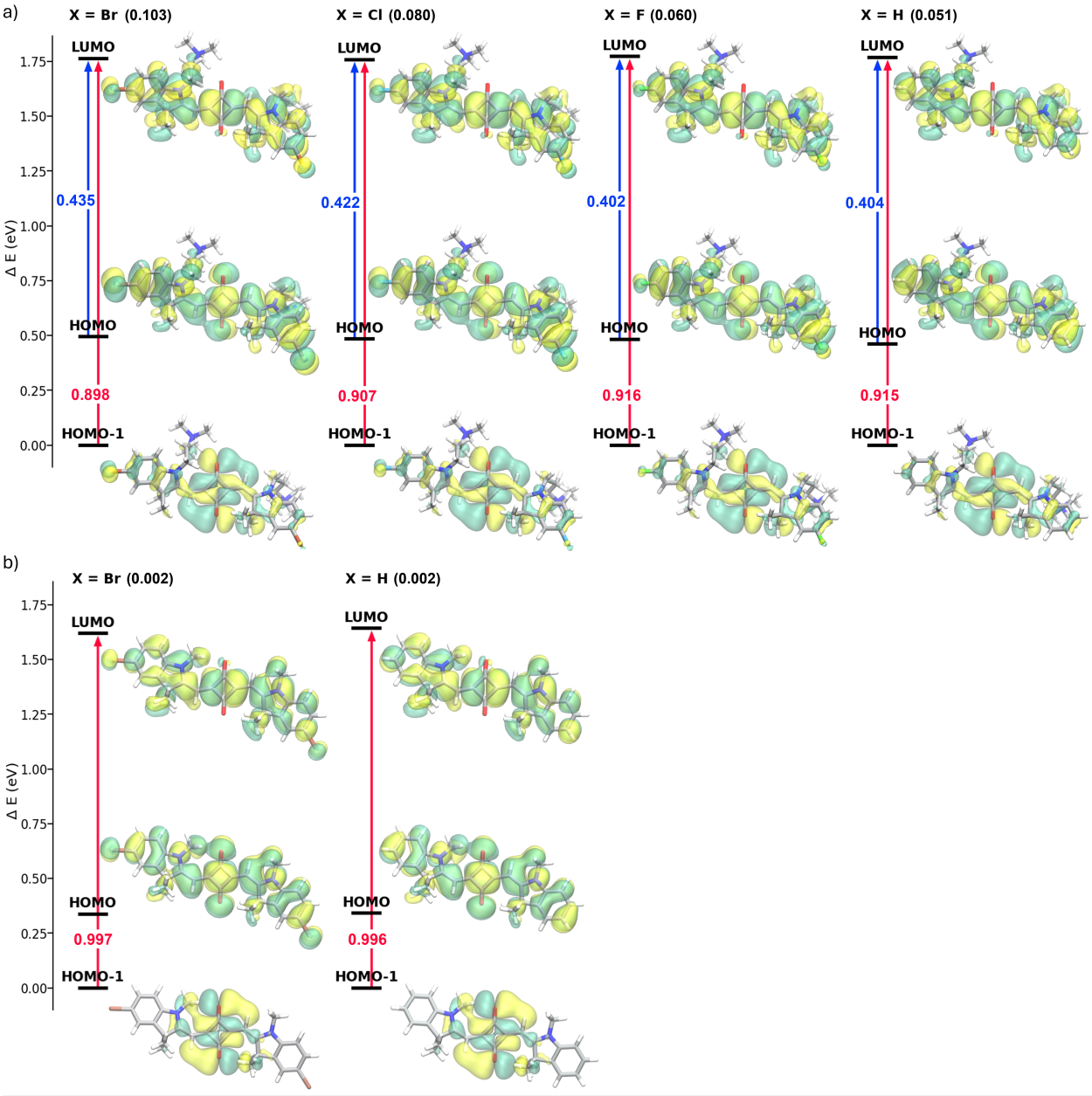

Figure 2.4: Molecular orbitals (MOs) of a) R = ETM and b) R = CH_3 squaraine analogs from DFT calculations with the PBE functional and 6-31+G* basis set. The labels for the blue and red arrows represent the MO transition amplitudes (X) contributing to S_1 (shown in the inset of Fig. 2.3). Oscillator strengths are given in parentheses.

2.5 Structural Flexibility of Squaraine Dyes

It was hypothesized that additional structural flexibility would enhance non-radiative relaxation, resulting in increased OA signal. Although the higher vibrational entropy calculated for the R = ETM analogs (Fig. 2.5) provides some support for this idea, these results are not necessarily conclusive as they do not directly account for the vibrational relaxation from the S_1 state. A future direction for this work would be to perform non-adiabatic molecular dynamics (NAMD) simulations, which would allow for the direct estimation of relaxation rate. During NAMD, normal mode tracking could be used to identify vibrational motions that facilitate non-radiative relaxation, leading to insights on what modifications could enhance OA signal generation.

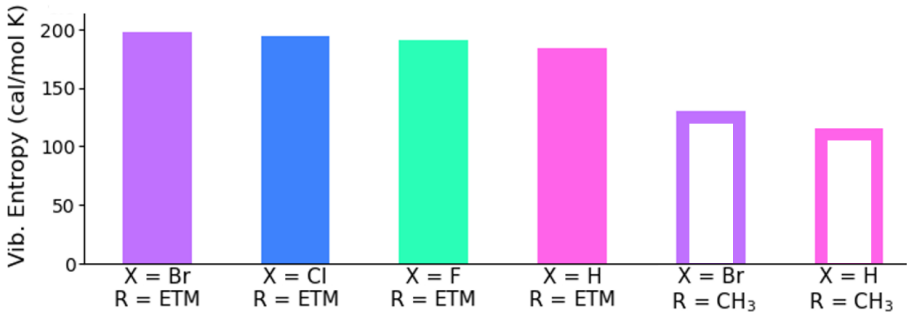

Figure 2.5: Vibrational entropy of squaraine analogs calculated using the PBE functional and 6-31+G* basis set. Adapted from ref 3.

2.6 Conclusion

This study provides theoretical insight into the structure-function relationships of OA signal generation. The intensity of the MSOT signal generated by a very weak absorption suggests that the squaraine analogs with flexible side chains efficiently convert photoexcitation into thermal energy. Results of MO analysis indicate that absorption could be tuned further towards the NIR region through variation of R-groups, and possibly increased by asymmetrical

substituents. While vibrational entropy calculations provided a quantitative measure of the effect of the ETM R-group on vibrational motions, it cannot yet be stated with certainty that these would result in increased non-radiative relaxation. Thus, the structural flexibility of OA imaging probes presents an excellent opportunity for further study utilizing NAMD simulations to assess the role of vibrational modes (especially low-frequency ones) during non-adiabatic transitions.

As the clinical application OA imaging is a relatively new field of interest, few computational studies have been published in this area. Detailed analysis of how structural modifications effect absorption and relaxation mechanisms could provide insights not only for the development of OA imaging dyes, but for other fields of probe development as well.

Chapter 3

A Computational Modeling of ADLumin Chemiluminescence: Oxygenation and Dioxetanone Formation

This chapter is adapted from:[38]

Wickizer, C.; Lander, C.; Pei, Z.; Yip, W. T.; Ran, C.; Shao, Y. A Computational Modeling of ADLumin Chemiluminescence: Oxygenation and Dioxetanone Formation. *J. Comput. Chem.* **2026**, *47*, e70372. DOI: 10.1002/jcc.70372.

3.1 Introduction

The development of molecular probes is critical for the advancement of *in vivo* optical imaging (OI), which is a cost-efficient complement to magnetic resonance imaging (MRI), computed tomography, and other imaging modalities. However, clinical applications of OI can be limited by photon penetration depth. In the case of fluorescence imaging (FLI), various interactions with tissue, such as surface reflection, scattering, absorption, and autofluorescence result in only 0.001-0.01% of incident photons reaching the detector.[39,40] While interference from biological tissues can be mitigated with near-infrared fluorescence (NIRF), the need for an external light source significantly reduces the signal-to-noise ratio (SNR). Compared to NIRF, substantially higher SNRs can be achieved with "molecularly generated light imaging",[14,41,42] especially bioluminescence (BL) and chemiluminescence (CL) in

which molecules undergo a chemical reaction to reach their electronic excited state and emit a photon upon relaxation to the electronic ground state.[22,43,44] As such, CL and BL offer two key advantages over NIRF and other OI imaging techniques: 1) the "one-way" photon trip increases penetration depth while maintaining a high SNR, and 2) they could acquire inherent target specificity from the need for a small-molecule "trigger" to initiate the chemical reaction[45,46] or a biomolecule to substantially enhance the output light signal. In the latter case, an especially promising "biosensor" application is the detection of amyloid beta (Aβ) plaques, a biomarker in the brains of patients with Alzheimer's disease (AD) that can begin to accumulate up to 30 years before the onset of memory loss, cognitive decline and other emotional / behavioral symptoms.[47]

Unlike BL reporters such as the well-known firefly luciferin/luciferase,[42,48–50] CL is generated from excited-state intermediates formed during chemical reactions that do not require catalyzing enzymes.[40] Although CL reactions are most commonly triggered by reactive oxygen or nitrogen species,[51–54] recent modifications to Schapp's 1,2-dioxetanes[17] have enabled the use of a variety of analyte-responsive groups.[16,21,23,48] Similarly, Cypridina luciferin analogs based on the imidazopyrazinone (IPO) skeleton[55] are responsive to molecular O_2. The autoxidation of IPO-based probes is strongly dependent on substituent groups,[55] as well as environmental characteristics, such as solvent and pH.[56–59] These properties were utilized to design turn-on probes, such as ADLumin-1 (Fig. 3.1), a CL probe that reacts with O_2 and produces amplified emission in the presence of Aβ aggregates.[5]

More recently, there has been further advances in the design of CL probes for the detection of Aβ aggregates associated with Alzheimer's disease.[4] It was hypothesized that the amplification of emission from ADLumin-1 is likely due to structural stabilization of the molecule by Aβ aggregates. Nevertheless, the rotation of the multiple conjugated double bonds in the molecule might still allow for some flexibility and lead to alternate excitation

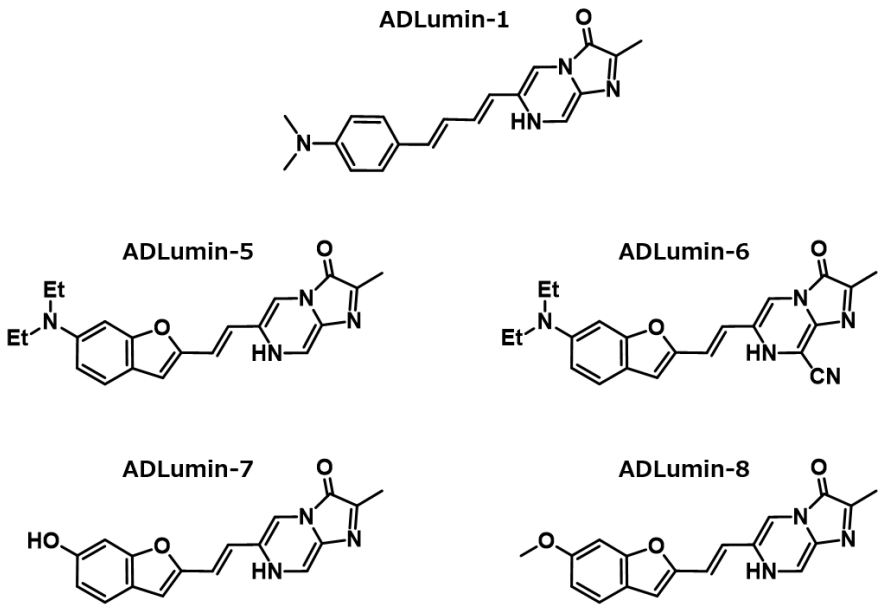

Figure 3.1: Structures of ADLumin-X analogs[4,5]

energy loss through non-radiative relaxation pathways. Accordingly, the bridging carbon chain of ADLumin-1 was fused into a furan ring in ADLumin-Xs (Fig. 3.1: X= 5, 6, 7, and 8) in order to reduce the flexibility and improve CL quantum yield (QY). The placement of an electron-withdrawing (cyano) group on the IPO moiety of ADLumin-6 extended the emission wavelength to 600 nm (*cf.* ∼540 nm for ADLumin-1 and ADLumin-5), but the output CL signal was reduced significantly. Furthermore, to probe the role of substituents on the benzofuran moiety, the diethylamino group of ADLumin-1, 5, and 6 was replaced with -OH and -OMe in ADLumin-7 and -8, respectively, but it also led to reduced QY. Among these newer ADLumin molecules, ADLumin-5 showed superior performance, with a higher *in vivo* radiance strength and a 1.5-fold signal amplification when imaging 5xFAD compared to wild-type mice.[4]

Following these developments in ADLumin-X probes, here we shall seek to gain more mechanistic insight into ADLumin-5 chemiluminescence. Generally, the CL mechanisms of IPO-based probes like ADLumin-5 consist of four steps illustrated in Fig. 3.2: (1) autoxidation (*i.e.* oxygenation) with O_2. It was suggested that a deprotonated IPO reactant (in its singlet ground state) undergoes a single electron transfer (SET) to triplet O_2, forming a diradical complex consisting of an oxidated IPO and the superoxide anion $O_2{}^{\cdot}-$.[4,60] Subsequently, the system undergoes a triplet–to–singlet spin–crossing during the C–O bond formation at one of the multiple sites at which $O_2{}^{\cdot}-$ can bind: C_8, C_2, and C_4 (I-1A, 1-1B, and I-1B' in Fig. 3.2, respectively). (2) intramolecular rearrangements. Regardless of the binding site, multiple intramolecular rearrangement steps (omitted from Fig. 3.2 for clarity) on the ground-state singlet surface are needed to reach the 1,2-dioxetanone intermediate. (3) decarboxylation to chemically excite the molecule, whereby the system proceeds through a conical intersection to the excited-state, open-ring product. (4) The system de-excites to emit a photon.

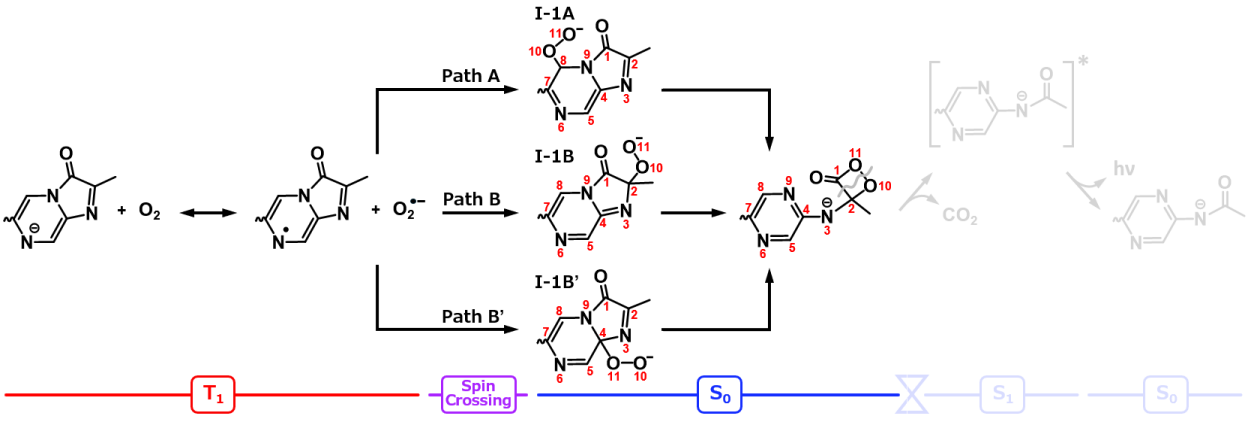

Figure 3.2: General reaction mechanism for ADLumin-5, abbreviated to show only the IPO core. Red numbers demonstrate the atom numbering scheme referred to in this work. Colored lines indicate the spin state of the system: initially a triplet (red), then undergoing a spin-crossing during C-O bond formation (purple) to form the singlet state first intermediate (I-1A, I-1B, or I-1B': blue). All paths undergo multiple intramolecular rearrangement steps (omitted) and eventually form the same 1,2-dioxetanone intermediate.

While the decomposition of 1,2-dioxetanones has been investigated for many chemiluminescent and bioluminescent systems,[61–70] the autoxidation mechanism of IPO-based molecules has been reported only a few times in recent literature. Early experiments on *Cypridina luciferin* and synthetic analogs suggested O_2 binding at C_8 or C_2 sites.[56,71–74] More recent computational investigations have focused primarily on O_2 binding at C_2 site.[68,75–77] Oxygenation at C_1 was also reported, but it was found to have a high energy barrier.[78] To our knowledge, oxygenation at C_4 has not been previously investigated and is a novel mechanism identified during the course of this work.

In this work, we focus on the steps of the CL mechanism of ADLumin-5 preceding the chemiexcitation, as indicated in Fig. 3.2. Specifically, we carry out a comprehensive density functional theory (DFT) study on the autoxidation and dioxetanone formation of ADLumin-5, with a discussion on the effects of substituents in the other ADLumin-X molecules.

3.2 Methods

We found in earlier study[4] that computed emission wavelengths for ADLumin-X open-ring products in the 180-U conformation (Fig. A.1) correlated well with experiment and were the most stable reactant conformations (Table A.2, A.3). In this work, thus, all ADLumin-X structures were modeled in the 180-U conformation. All calculations were carried out with Q-Chem 6.1[79] employing unrestricted density functional theory at the PBE0/6-31+G* level of theory.[32,34] To emulate experiments carried out *in vitro* with PBS (phosphate buffered saline) solvent, the reaction was modeled using the SMD continuum solvation model for water solvent.[80] Optimized intermediate and transition state (TS) structures were confirmed by numerical frequency calculations to have the correct number of imaginary frequencies (0 and 1, respectively). Minumim energy crossing points (MECPs) were located using Harvey's MECP search algorithm[81,82] as implemented in sobMECP.[83] The MECP search algorithm

minimizes the difference in energy between two states using two orthogonal gradients that will converge to zero at the MECP geometry. The gradient $\vec{f}$ minimizes the difference in energy between states, while the gradient $\vec{g}$ minimizes the energy in the branching space. The gradients are defined as

$$\vec{x}_1 = \left(\frac{\partial E_{\mathrm{S}}}{\partial \vec{q}}\right) - \left(\frac{\partial E_{\mathrm{T}}}{\partial \vec{q}}\right) \tag{3.1}$$

$$\vec{f} = (E_{\mathrm{S}} - E_{\mathrm{T}})\,\vec{x}_1 \tag{3.2}$$

$$\vec{g} = \left(\frac{\partial E_{\mathrm{S}}}{\partial \vec{q}}\right) - \frac{\vec{x}_1}{|\vec{x}_1|}\left[\left(\frac{\partial E_{\mathrm{S}}}{\partial \vec{q}}\right)\cdot\frac{\vec{x}_1}{|\vec{x}_1|}\right] \tag{3.3}$$

where $\vec{q}$ is the nuclear coordinates and S and T denote the singlet and triplet spin states, respectively.

3.3 ADLumin-5 Oxygenation

We studied the three aforementioned O_2 binding positions (C_8, C_2, and C_4) shown in Fig. 3.2, where each site initiates a separate reaction path (A, B, and B'), each eventually converging to the same 1,2-dioxetanone intermediate. Singlet and triplet surface minimum energy paths (MEPs) for the C–O bond formations were calculated by performing restrained geometry optimizations with the C–O bond distance gradually increased from the optimized geometries for the first intermediates (I-1A, 1-1B, and I-1B'). These MEPs are shown in Fig. 3.3, where the reaction coordinates correspond to the atom numbering system shown in Fig. 3.2. To afford a fair comparison between the paths, ΔE is calculated relative to the sum of the isolated reactant energies (singlet ADLumin-5 and $^3O_2$).

Minimum energy crossing point (MECP) searches along these surfaces yielded 2 distinct MECP structures: one for Path A (MECP-A, Fig. 3.3a), and another shared by Paths B and B' (MECP-B/B', Fig. 3.3b-c). MECP-A is lower in energy (7.4 kcal/mol) and has a C_8–O_{10}

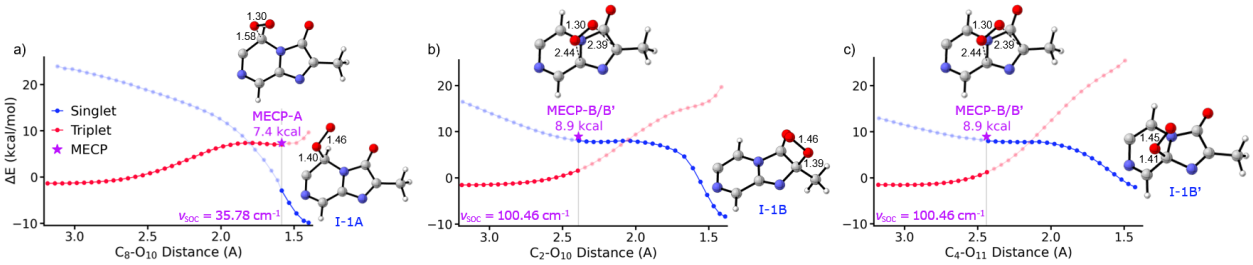

Figure 3.3: Singlet (blue) and triplet (red) potential energy surfaces, as well as minimum energy crossing points (MECP, purple) for O_2 binding to the ADLumin-5 reactant at three different sites: a) Path A, b) Path B, and c) Path B'. Reaction coordinates correspond to the atom numbering shown in Fig. 3.2. The structures are abbreviated to the IPO moiety for clarity. All energies are plotted relative to the same reactants: $^3O_2$ and singlet ADLumin-5 (R^-). Unrestricted DFT calculations were performed using PBE0 functional, 6-31+G* basis set, and SMD model for water.

distance of 1.58 Å. MECP-B/B' (8.9 kcal/mol) occurs earlier in the C–O bond formation process for both Path B (C_2–O_{10} = 2.39 Å) and Path B' (C_4–O_{11} = 2.44 Å). The O–O bond length is nearly the same for both MECP structures (1.30 Å), closely resembling that of the superoxide anion radical (1.33 Å, Fig. A.3). Towards further study of the single electron transfer (SET) mechanism previously proposed for cypridina luciferin,[4,55] we examined the O_2 ChElPG charges along the C–O bond formation coordinates (Fig. A.2), where all paths begin with a slightly negatively charged O_2. This suggests a charge-transfer interaction between ADLumin-5 and triplet oxygen that contributes to the negative ΔE value for C–O bond distances of 3.0-3.2 Å in all panels of Fig. 3.3.

3.4 ADLumin-5 Intramolecular Rearrangement

Following oxygenation, a series of intramolecular rearrangement steps brings the system to the dioxetanone intermediate that will eventually undergo chemiexcitation during decarboxylation. The energy profiles for each mechanism are shown in Fig. 3.4, where all energies are also plotted relative to the sum of the isolated reactants to provide a fair comparison. Structures and key bond distances are shown in Fig. 3.5. Our key findings on these three

reaction paths are as follows: 1) Path A has the highest energy transition state (TS-2A, 10.8 kcal/mol) and reaches the final intermediate in 3 steps, 2) Path B' converges to Path B, thus Path B' undergoes a total of 4 rearrangement steps, and 3) Path B generally has low barriers and requires only 2 steps to reach the final intermediate. Overall, the highest activation energy (E_a = 16.1 kcal/mol) was calculated for TS-2A, the only transition state involved in the breaking of two bonds (C–O and C–N bonds) at the same time (Fig. 3.5). Paths B' and B are connected in two ways: their first intermediates (I-1B and I-1B') share an MECP (MECP-B/B') along a bifuracting pathway, and the third intermediate for Path B' (I-3B') is identical to I-1B, indicating that Path B' is an alternative "precursor" route to Path B. The shared MECP indicates an equivalent barrier for oxygenation at C_2 and C_4, though I-1B' is the least stable I-1 (-2.1 kcal/mol as compared to -8.5 kcal/mol and -9.7 kcal/mol for I-B and I-1A, respectively) and has a thermally more accessible barrier for the reverse reaction to form either I-1B or I-1A.

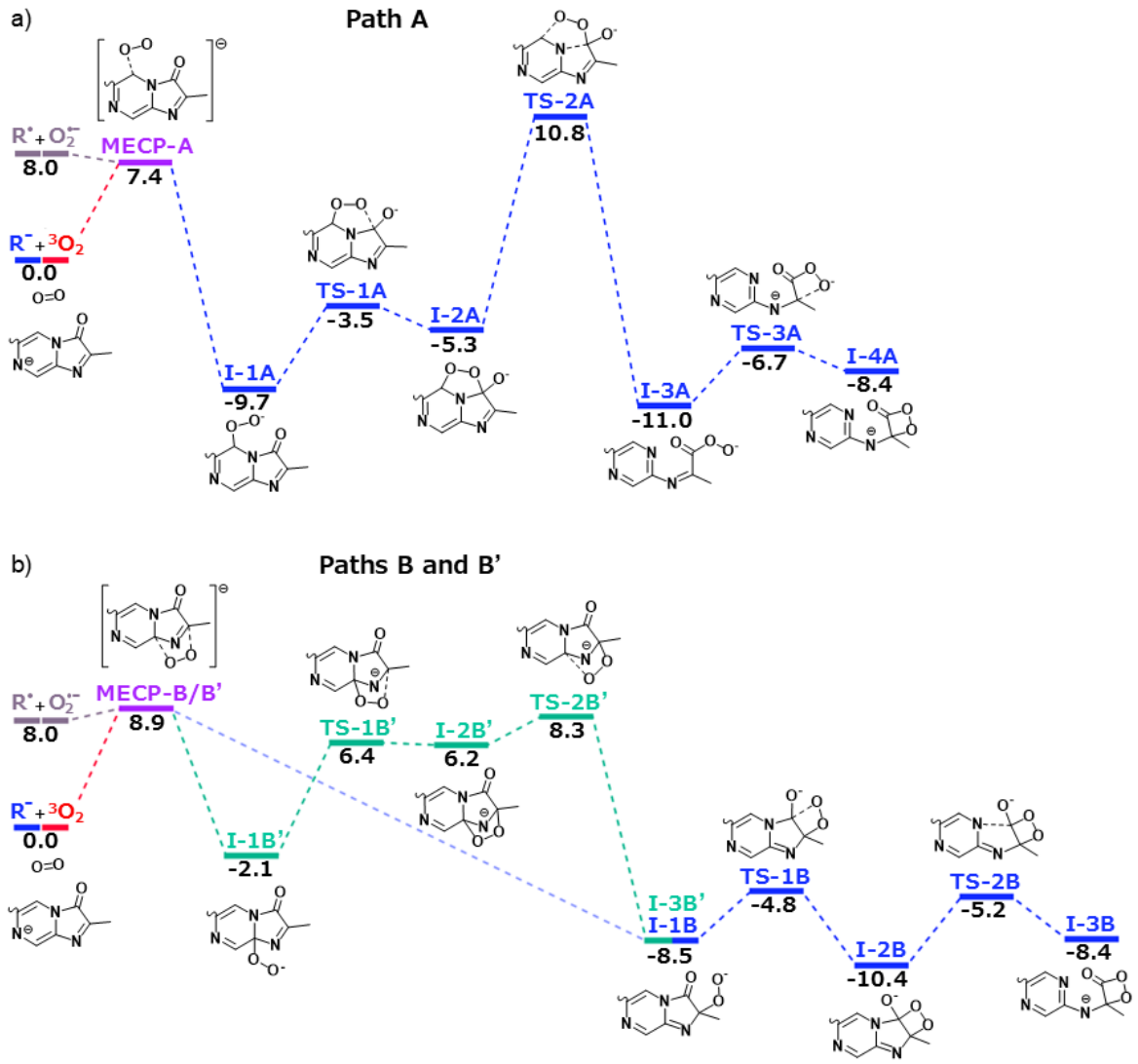

Figure 3.4: Calculated electronic energies (in kcal/mol) for ADLumin-5 reaction paths: a) Path A, b) Paths B and B'. I-4A and I-3B are identical, as are I-3B' and I-1B. The structures are abbreviated to the IPO moiety for clarity. All energies are plotted relative to the same reactants: $^3O_2$ and singlet ADLumin-5 (R^-). Unrestricted DFT calculations were performed using PBE0 functional, 6-31+G* basis set, and SMD model for water.

The geometries, relevant bond distances, and energy differences for the three paths are shown in Fig. 3.5. The first transition states all involve the formation of the second C–O bond, with the most favorable (TS-1B) connecting the oxygen to a carbon atom adjacent to the initial binding site. In contrast, bridging across multiple atoms causes a distortion of

the IPO in I-2A and to a larger degree in I-2B', which has a higher energy than other second intermediates (I-2A and I-2B). TS-2A and TS-2B' both involve C–O bond dissociations and are much higher in energy than TS-2B, which involves a C–N bond dissociation that brings Path B to the final intermediate (I-3B). Path A requires an additional step to reach the same final intermediate through the closure of the 1,2-dioxetanone seen in TS-3A. The most favorable mechanism thus proceeds through Path B, which has the fewest and generally lower barrier rearrangement steps.

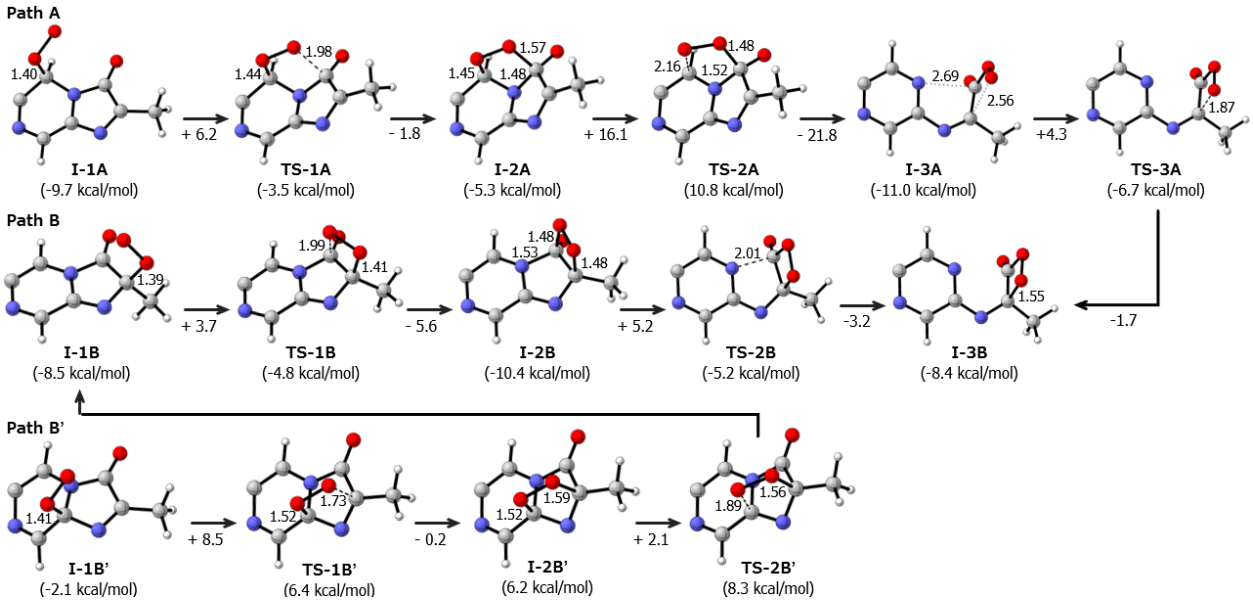

Figure 3.5: ADLumin-5 intermediate and transition state geometries with bond distances and energy changes (in kcal/mol) for Paths A (top), Path B (middle), and Path and B' (bottom). The structures are abbreviated to the IPO moiety for clarity. Unrestricted DFT calculations were performed using PBE0 functional, 6-31+G* basis set, and SMD model for water.

3.5 Comparison of Key Reaction Steps for ADLumin-X Molecules (X = 5, 6, 7, and 8)

To investigate the effects of substituents on the autoxidation mechanism, the same reaction pathways were calculated for the other ADLumin-X molecules (Fig. A.4). While the

ADLumin-5 structures were used to build initial geometries, all structures were re-optimized and verified to have the correct number of imaginary frequencies. The highest energy barrier steps for each path are shown in Fig. 3.6, where the energies for each molecule are plotted relative to their corresponding reactant. ADLumin-8 is omitted from Fig. 3.6 as the energy profile is nearly identical to ADLumin-7 (Table A.4, Fig. A.4). Substituents on the benzofuran (ADLumin-7 and -8) had minimal effect on the mechanisms as the autoxidation takes place entirely on the IPO moiety. In contrast, the electron-withdrawing (cyano) group on the IPO moiety had a substantial impact on the energy profiles for all paths. Most notably, relative to ADLumin-5, the ADLumin-6 MECP-A is lowered significantly while MECP-B/B' is raised. This indicates a stronger preference for O_2 binding to C_8, which is only slightly favored for ADLumin-5. In addition, the stabilization of I-2A would further slow down the forward/backward reactions from this intermediate. While the energy barriers were actually lowered for TS-1B' and TS-2B with ADLumin-6, a deeper energetic well of I-2A and higher energy MECP-B/B' likely negate the effects this would have on the overall rate.

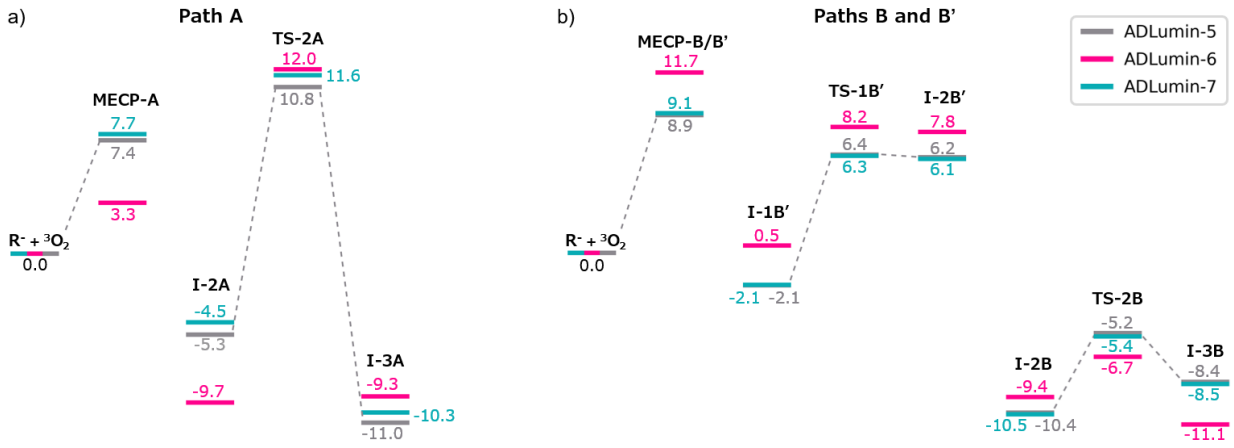

Figure 3.6: Comparison of high-barrier steps for ADLumin-5 to the same reaction steps calculated for ADLumin-6 and -7. a) Path A, b) Paths B and B'. All energies are plotted relative to their respective reactants ($^3O_2$ and singlet ADLumin-X). The full pathways are shown in Fig. S4. Unrestricted DFT calculations were performed using PBE0 functional, 6-31+G* basis set, and SMD model for water.

The MECP structures are compared for ADLumin-5, 6, and 7 in Fig. 3.7. The significant decrease in the MECP-A energy for ADLumin-6 can be explained by the orientation of the unbound O atom, which closely resembles the I-1A structure of ADLumin-5. In contrast, the O_2 molecule is oriented horizontally in MECP-A for ADLumin-5 and -7 and must rotate to form I-1A. The MECP-B/B' structures are similar, though ADLumin-6 has slightly shorter C–O distances, resulting in an increase in energy (2.8 kcal/mol) relative to ADLumin-5. This effect is more pronounced at C_4, which is closer to the cyano group; 1-1B' for ADLumin-6 was destabilized to a similar degree (2.6 kcal/mol).

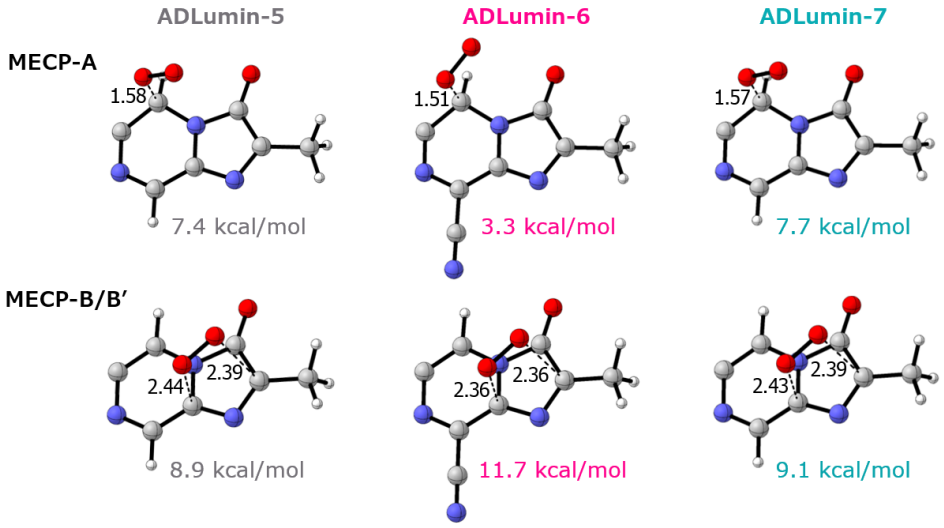

Figure 3.7: Comparison of ADLumin-5, ADLumin-6, and ADLumin-7 MECP-A and MECP-B/B' structures (abbreviated to the IPO moiety). Unrestricted DFT calculations were performed using PBE0 functional, 6-31+G* basis set, and SMD model for water.

3.6 Discussion

This work details three competing mechanisms for the autoxidation of deprotonated ADLumin-X dyes in water. While reports could only be found for the most efficient of these (Path B), a quantitative comparison to previous theoretical studies on IPO-based chemiluminescent probes[73,77,78] could provide insight into the effects of protonation state,

substituent groups, and solvent molecules on the IPO core functionality. Compared to the neutral form, anionic coelenterazine (CTZ) derivatives may be more affected by solvent polarity[73] and have been found to undergo autoxidation more readily when modeled with[77] and without solvent.[78]

Our mechanism for Path B most closely resembles that published by Ding *et al.* for CTZ[78] – both include an initial open-ring peroxide intermediate, followed by a stepwise 4-membered ring closure and dissociation of C_1–N_9 to form the dioxetanone (I-3B). In contrast, Xie *et al.* found a concerted mechanism for I-3B formation from an open-ring peroxide;[68] a similar mechanism was reported by Isobe *et al.*,[73] as well as a "gauche-in" conformation that bypasses the open-ring peroxide altogether. In the bisdeoxycoelenterazine (bis-CTZ) and Diphenylterazine (DTZ) autoxidation mechanisms published by Yeh *et al.*,[77] the final ground-state intermediate resembles I-2B, rather than I-3B.

3.7 Conclusion

In this work, we focus on ADLumin-5, which is a bright, turn-on chemiluminescent probe for the detection of Aβ aggregates and represents a great step towards *in vivo* clinical detection of biomarkers of Alzheimer's disease. We aim to provide theoretical insights into multiple factors governing the chemiluminescent efficiency of ADLumin probes. Specifically, our key findings are as follows:

- The autoxidation and 1,2-dioxetanone formation of ADLumin-5 proceed through multiple competing pathways, with Path B being the most kinetically favorable.
- While oxygenation is not strongly favored for any specific position, the more complex mechanisms and higher energy intermediates for Paths A and B' likely contribute less to the chemiluminescent quantum yield of ADLumin-5.

- The electron-withdrawing cyano substituent at C_5 of ADLumin-6 induces a preference for oxygenation at C_8, which leads to a thermally inaccessible energy barrier in Path A.
- -OH and -OMe substituents on the benzofuran (ADLumin-7 and -8, respectively) had little impact on the energetics of the predicted reaction paths.

Related to the last two findings, our results indicate that while the low quantum yield of ADLumin-6 can potentially be attributed to a slower autoxidation reaction, the same cannot be said for ADLumin-7 and -8. The combined results of this work and Ran et al. suggest that substituents not directly attached to the IPO moiety could have a significant impact on chemiexcitation.

Looking forward, we are following others in the community[62,64,65,75,77,78,84] to investigate the decomposition mechanism of 1,2-dioxetanones, which is important as cyclic peroxides have become a common feature among many CL and BL molecules.[85] The dynamical surface crossing around the S_0-S_1 conical intersection will be the main focus of our exploration of the chemiexcitation mechanisms of ADLumin-X molecules. Currently, work is also underway on a spin-adiabatic model of the spin-crossing oxygenation reaction, which accounts for spin-orbit coupling and can provide a fuller description of the oxygenation.

Overall, we hope that the work we present here aids in understanding not only the chemiluminescence mechanisms of ADLumin-X molecules, but also other IPO-based reporters

Chapter 4

A Computational Modeling of ADLumin Chemiluminescence: Chemiexcitation and Photon Emission

4.1 Introduction

In chemiluminescent reactions, chemiexcitation occurs via a conical intersection (CI) between the ground (S_0) and first excited state (S_1). Imidazopyrazinone (IPO)-based CL molecules undergo chemiexcitation through thermolysis of the 1,2-dioxetanone.[66,68,86] Studies have found that deprotonated IPOs tend to have lower energy barriers compared to protonated counterparts.[68,86] Several mechanisms for the decomposition of the 1,2-dioxetanone ring have been investigated, including chemically initiated electron exchange luminescence (CIEEL),[87,88] charge transfer induced luminescence (CTIL),[69,73,75,89] and charge transfer induced decomposition (CTID).[90–92] Amongst these, a theoretical study by the Liu group provided strong support for a gradually reversible CTIL mechanism in firefly dioxetanone (FDO^-)[67] involving two separate conical intersections (CIs) for the O–O and C–C bond cleavages. In this section, we follow that work and focus on the decomposition of a similar dioxetanone ring and emission of ADLumin-5.

4.2 Chemiexciation: S_0/S_1 Conical Intersection

This section presents our preliminary results for the dioxetanone decomposition of ADLumin-5. The firefly dioxetanone decomposition mechanism identified by the Liu group[67] was reproduced as a test case for validating the methods used in our study.

4.2.1 Methods

All calculations were carried out using the Q-Chem 6.4 software package.[35] Ground state unrestricted density functional theory optimizations were performed using the PBE0 functional[33] with the D3(BJ) dispersion correction[93] and 6-31G** basis set.[34] Mixed-reference spin-flip time-dependent density functional theory (MRSF-TDDFT) single point calculations were performed using the BHHLYP functional[94] and 6-31G** basis set. The SMD continuum solvation model for water solvent[80] was used for all ADLumin-5 calculations, while FDO^- was modeled without solvent.

4.2.2 Results

The dioxetonane decomposition pathways obtained for FDO^- and ADLumin-5 are shown in Fig. 4.1. For FDO^-, a smooth intrinsic reaction coordinate (IRC) pathway was obtained starting from the $TS_{O\text{-}O}$ geometry from ref. 67. Using these ground state geometries, MRSF-TDDFT single point energies clearly show the nearly degenerate S_0 and S_1 energies at $CI_{O\text{-}O}$ and $CI_{C\text{-}C}$. A similar $TS_{O\text{-}O}$ structure was created for ADLumin-5, though an IRC connecting the closed and open dioxetanone rings could not be obtained. Instead, the ground state reaction path for the dioxetonane decomposition of ADLumin-5 was obtained via the freezing string method (FSM).[95] Upon stretching the O-O bond, spin-restricted DFT calculations became unstable due to spin contamination, resulting in the discontinuities shown in Fig. 4.1b. MRSF-TDDFT calculations show a near S_0/S_1 degeneracy at 3.5 Å; this structure is

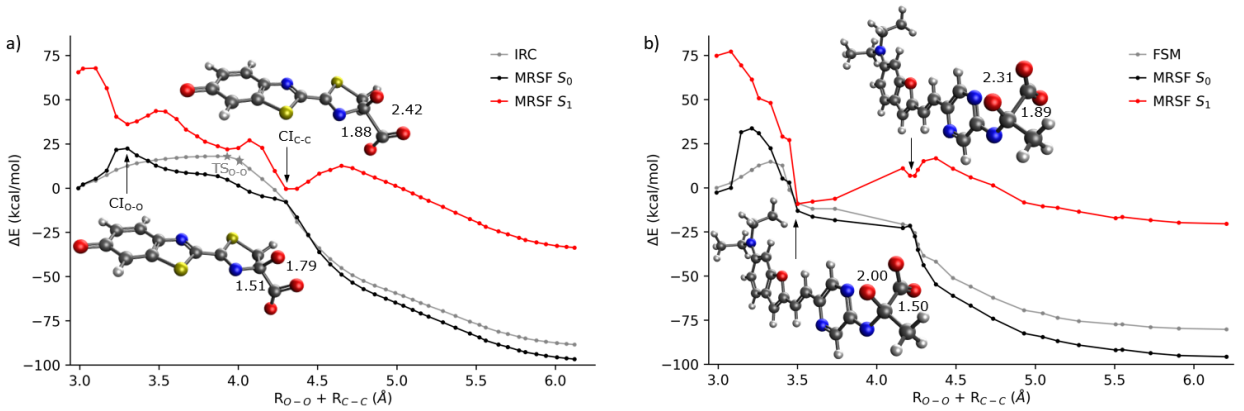

Figure 4.1: Dioxetonane decomposition pathways obtained for a) FDO^- and b) ADLumin-5. Shown in gray are ground state reaction paths acquired at the PBE0-D3(BJ)/6-31G** level of theory. The MRSF-TDDFT S_0 and S_1 energies calculated at the BHHLYP/6-31G** level of theory are shown in black and red. The SMD solvent model was used for ADLumin-5, while FDO^- was modeled in the gas phase.

similar to $CI_{O\text{-}O}$ of FDO^-, though with a longer O-O distance. Additionally, a small dip in S_1 energy at 4.2 Åfor ADLumin-5 resembles the S_1 topology seen around $CI_{C\text{-}C}$ of FDO^-. However, due to the difficulties in calculating the ADLumin-5 ground state reaction path with DFT, an accurate comparison of the ADLumin-5 and FDO^- dioxetonane decomposition mechanisms has not yet been made.

4.3 Photon Emission: Effect of Structural Modifications on Emission Wavelengths

This section is adapted from:[4]

Zhang, J.; Wickizer, C.; Ding, W.; Van, R.; Yang, L.; Zhu, B.; Yang, J.; Wang, Y.; Wang, Y.; Xu, Y.; Zhang, C.; Shen, S.; Wang, C.; Shao, Y.; Ran, C. In vivo Three-Dimensional Brain Imaging with Chemiluminescence Probes in Alzheimer's Disease Models. *Proc. Natl. Acad. Sci.* **2023**, *120*, e2310131120, DOI: 10.1073/pnas.2310131120.

4.3.1 Methods

DFT and TDDFT calculations were performed using the Q-Chem 5.2 software package[35] All calculations were performed using the conductor-like polarizable continuum model (C-PCM)[96] with the dielectric constant of DMSO(46.7); in addition, the optical dielectric constant of DMSO (2.18) was used for the absorption (i.e., vertical excitation) energy calculations. For each molecule, the ground-state geometry was optimized using DFT with the ωB97X-D functional[97] and 6-31+G* basis set.[34] At the optimized geometries, TDDFT calculations were performed using the same functional and basis set to obtain vertical excitation energies. For each molecule, the lowest-energy excited state with a significant oscillator strength (greater than 0.7) was chosen to analyze absorption peaks and as the initial state for subsequent emission wavelength calculations. For the emission spectra calculations, we started from the ground-state geometries and performed further geometry optimization on the chosen excited state potential energy surface. In order to ensure the optimization proceeded on the same surface, we used the state tracking algorithm implemented in Q-Chem, which is based on the transition density overlap in the atomic orbital (AO) representation between consecutive geometries.

$$S_{12}^{ij} = \mathrm{Tr}(\mathbf{R}_1^i \mathbf{S}_{12} \mathbf{R}_2^{j\top} \mathbf{S}_{21}) \tag{4.1}$$

Here, $\mathbf{S}_{12}$ and $\mathbf{S}_{21}$ are the overlap matrice between basis functions at the two geometries and its tranpose, $\mathbf{R}_1^i$ is the transition density matrix for the excitation from the ground state to the i-th excited state at the previous geometry, $\mathbf{R}_1^i = \mathbf{C}_{\mathrm{v},1} \left(\mathbf{X}_{i,1} + \mathbf{Y}_{i,1}\right) \mathbf{C}_{\mathrm{o},1}^\top$, and $\mathbf{R}_2^{j\top}$ is the transposed transition density matrix for excitation to state j at the current geometry, $\mathbf{R}_2^j = \mathbf{C}_{\mathrm{v},2} \left(\mathbf{X}_{j,2} + \mathbf{Y}_{j,2}\right) \mathbf{C}_{\mathrm{o},2}^\top$. The HOMO-LUMO energy gaps shown in Fig.4.3 were calculated at the optimized excited state geometries.

4.3.2 Results

Experimental evidence indicates that ADLumin-5 has a slight peak in chemiluminescence at a pH of 3, and intensifies above pH 7.4.[4] While the anionic ADLumin reactant is thought to undergo oxygenation and dioxetanone formation, it is possible that protonation occurs prior to photon emission as depicted in Fig. 4.2a. Additionally, the open ring product could also be protonated in solution following the CL reaction. Indeed, the significant red shift of experimentally measured fluorescence (FL) compared to CL wavelengths suggests emission from two different species. As such, both neutral and anionic ADLumin-X analogs (X = 5-8) were modeled in the lowest energy 180-U conformation (Fig. A.1 and Table A.2). The calculated emission wavelengths of the anionic species are plotted against the experimental CL wavelengths in Fig. 4.2a, while calculated emission wavelengths of the neutral species are shown in Fig. 4.2b against the experimental FL wavelengths.

Table 4.1: Experimentally measured fluorescence and chemiluminescence wavelengths, as well as calculated emission wavelengths for neutral and anionic ADLumin open ring products. Calculations were performed using the ωB97X-D functional, 6-31+G* basis set, and PCM model for DMSO. Adapted from ref 4.

	Experiment		Calculated	
X	Chemiluminescence	Fluorescence	$[\text{ADLumin-X(O)}]^-$	ADLumin-X(O)
5	544	588	540	556
6	593	617	555	586
7	474	497	516	496
8	457	489	517	499

While the emission wavelengths calculated for the anionic $[\text{ADLumin-X(O)}]^-$ (Fig. 4.2b and Table 4.1) are red shifted compared to neutral ADLumin-7(O) and ADLumin-8(O), the opposite is true for ADLumin-5(O) and ADLumin-6(O). Thus, it is not possible to conclude from this comparison which species is responsible for the CL emission. In both cases, the trend in calculated emission wavelengths among analogs of different X-groups aligns well with the experimentally observed trend.

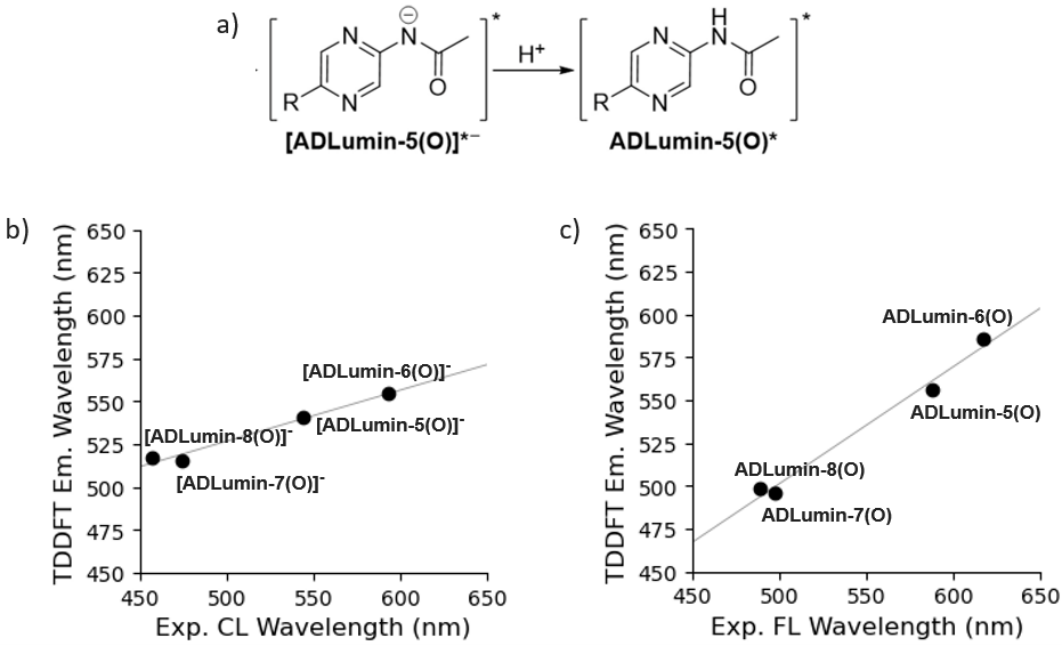

Figure 4.2: a) Anionic and neutral forms of the ADLumin-5 open ring product. b) Calculated emission wavelengths for anionic ADLumin products plotted against the experimentally measured chemiluminescence wavelengths. c) Calculated emission wavelengths for neutral ADLumin products plotted against the experimentally measured fluorescence wavelengths. Calculations were performed using the ωB97X-D functional, 6-31+G* basis set, and PCM model for DMSO. Adapted from ref 4.

The strategic placement of functional groups with electron donating or withdrawing capabilities can be used to alter orbital energies and tune absorption or emission wavelengths. The [ADLumin-X(O)]$^-$ molecules are a good demonstration of this principle, as our results indicate that only a HOMO–LUMO transition is involved in the emission (Fig. 4.3, the correlation between orbital energies and excitation energy is relatively straightforward. The longest emission wavelength was observed for [ADLumin-6(O)]$^-$, which can be attributed to stabilization of the LUMO due to the electron withdrawing cyano group on the IPO moiety (Fig. 4.3). Interestingly, electron donating groups (EDGs) on the phenyl of the benzofuran had an even more substantial effect on emission wavelengths. Though the -OH and -OMe groups of [ADLumin-7(O)]$^-$ and [ADLumin-8(O)]$^-$ aren't typically considered to be substantially stronger EDGs than -NR_2, the combination of HOMO stabilization and LUMO

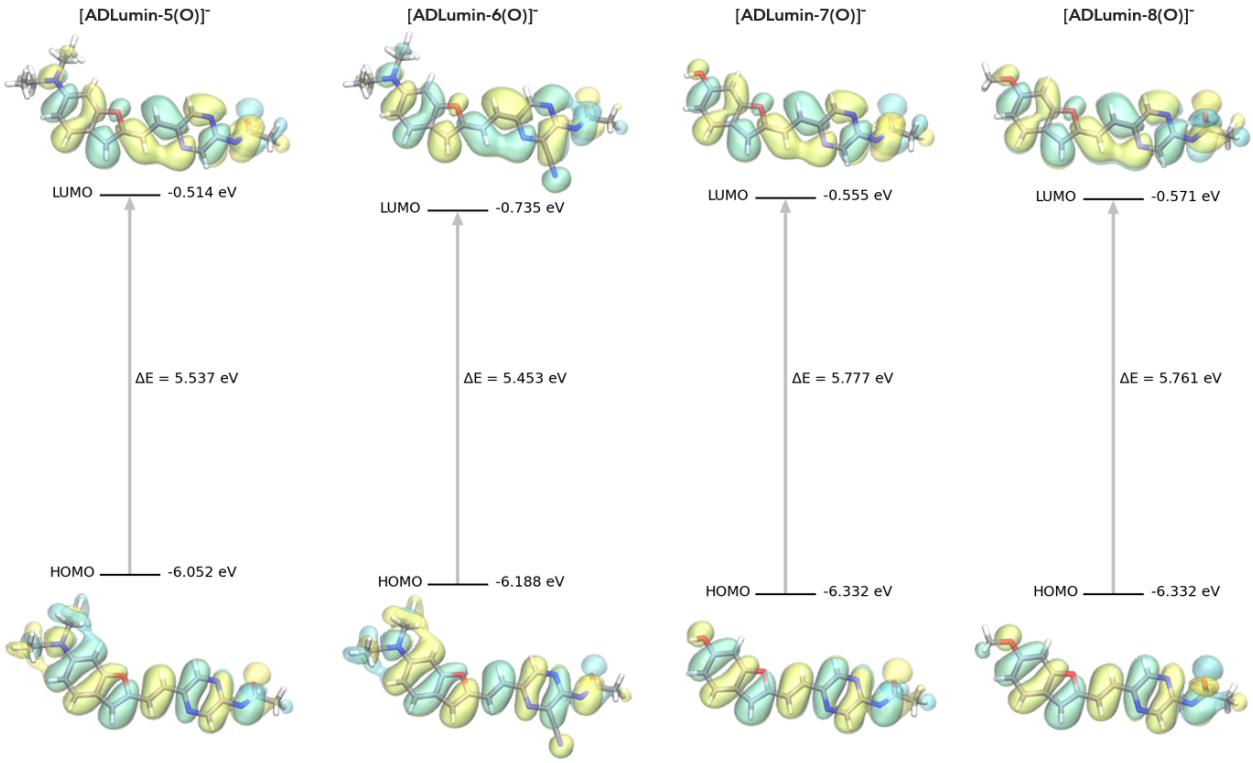

Figure 4.3: HOMO-LUMO gaps for the anionic ADLumin-X open ring products. DFT calculations were performed using the ωB97X-D functional, 6-31+G* basis set, and PCM model for DMSO. Adapted from ref 4.

destabilization resulted in signifantly shorter emission wavelengths relative to [ADLumin-5(O)]$^-$. Similar trends were observed for the protonated ADLumin-X open ring products (ADLumin-X(O), Fig. A.5).

4.4 Conclusion

In this work, we focus on the chemiexcitation portion of the ADLumin-5 chemiluminescence mechanism, as well as the effects of structural modifications on photon emission. Chemiexcitation was examined through an effort to locate the CI(s) that occur during decomposition of the dioxetanone ring. While it is not clear yet why the methodology applied to FDO$^-$ does not yield a similar reaction pathway for ADLumin-5, a more accurate pathway may be

obtained once optimizations at the MRSF-TDDFT level of theory are available.

Photon emission was examined via TDDFT calculations of emission wavelengths from relaxed excited-state geometries. The red shift caused by an electron-withdrawing IPO substituent was attributed to stabilization of the LUMO, while larger blue shifts observed for electron-donating benzofuran substituents were caused by effects on both the HOMO and LUMO. While the oxygenation and dioxetanone formation processes discussed in Chapter 3 occur on the IPO moiety, the results discussed here indicate that functionalization of the benzofuran may be more suitable for tuning emission wavelength without compromising reaction rate.

The delocalization of the frontier MOs suggests that it may be fruitful to examine the effects of structural modifications on chemiexcitation, as barriers to CIs would also impact the chemiluminescent efficiency. Once methodology for modeling the ADLumin-5 dioxetanone decomposition mechanism is established, a logical next step would be to extend this approach to ADLumin-6, -7, and -8. Non-adiabatic molecular dynamics simulations will be necessary to study the rates of surface crossing events, including relaxation mechanisms, as well as the mechanism by which $A\beta$ aggregates enhance chemiluminescence.

Bibliography

[1] Catana, C.; Drzezga, A.; Heiss, W.-D.; Rosen, B. R. PET/MRI for Neurologic Applications. *J. Nucl. Med.* **2012**, *53*, DOI: 10.2967/jnumed.112.105346.

[2] Lee, S.; Kim, E. E.; Nakata, H.; Lee, S.; Choi, C. H. Efficient implementations of analytic energy gradient for mixed-reference spin-flip time-dependent density functional theory (MRSF-TDDFT). *J. Chem. Phys.* **2019**, *150*, 184111, DOI: 10.1063/1.5086895.

[3] MacCuaig, W. M.; Wickizer, C.; Van, R. S.; Buabeng, E. R.; Lerner, M. R.; Grizzle, W. E.; Shao, Y.; Henary, M.; McNally, L. R. Influence of structural moieties in squaraine dyes on optoacoustic signal shape and intensity. *Chem* **2024**, *10*, 713–729, DOI: 10.1016/j.chempr.2023.11.016.

[4] Zhang, J.; Wickizer, C.; Ding, W.; Van, R.; Yang, L.; Zhu, B.; Yang, J.; Wang, Y.; Wang, Y.; Xu, Y.; Zhang, C.; Shen, S.; Wang, C.; Shao, Y.; Ran, C. In vivo Three-Dimensional Brain Imaging with Chemiluminescence Probes in Alzheimer's Disease Models. *Proc. Natl. Acad. Sci.* **2023**, *120*, e2310131120, DOI: 10.1073/pnas.2310131120.

[5] Yang, J.; Yin, W.; Van, R.; Yin, K.; Wang, P.; Zheng, C.; Zhu, B.; Ran, K.; Zhang, C.; Kumar, M.; Shao, Y.; Ran, C. Turn-on Chemiluminescence Probes and Dual-Amplification of Signal for Detection of Amyloid Beta Species in vivo. *Nat. Commun.* **2020**, *11*, 4052, DOI: 10.1038/s41467-020-17783-4.

[6] Rieffel, J.; Chitgupi, U.; Lovell, J. F. Recent Advances in Higher-Order, Multimodal, Biomedical Imaging Agents. *Small* **2015**, *11*, 4445–4461, DOI: 10.1002/smll.201500735.

[7] García-Figueiras, R.; Padhani, A. R. In *Functional Imaging in Oncology: Biophysical Basis and Technical Approaches - Volume 1*; Luna, A., Vilanova, J. C., Hygino da

Cruz Jr., L. C., Rossi, S. E., Eds.; Springer: Berlin, Heidelberg, 2014; pp 77–96, DOI: 10.1007/978-3-642-40412-2_5.

[8] Chen, Z.; Deán-Ben, X. L.; Gottschalk, S.; Razansky, D. Hybrid system for in vivo epifluorescence and 4D optoacoustic imaging. *Opt. Lett.* **2017**, *42*, 4577–4580, DOI: 10.1364/OL.42.004577.

[9] Li, H.; Zhang, M.; Lin, Z.; Deng, Z.; Cao, C.; Zhan, S.; Liu, W.; Sun, B. Utility of hybrid PET/MRI in stereoelectroencephalography guided radiofrequency thermocoagulation in MRI negative epilepsy patients. *Front. Neurosci.* **2023**, *17*, 1163946, DOI: 10.3389/fnins.2023.1163946.

[10] Bell, A. G. On the production and reproduction of sound by light. *American Journal of Science* **1880**, *s3-20*, DOI: 10.2475/ajs.s3-20.118.305.

[11] Manohar, S.; Razansky, D. Photoacoustics: a historical review. *Adv. Opt. Photon.* **2016**, *8*, 586–617, DOI: 10.1364/AOP.8.000586.

[12] Deán-Ben, X. L.; Gottschalk, S.; Larney, B. M.; Shoham, S.; Razansky, D. Advanced optoacoustic methods for multiscale imaging of in vivo dynamics. *Chem. Soc. Rev.* **2017**, *46*, 2158–2198, DOI: 10.1039/C6CS00765A.

[13] Blau, R.; Shelef, O.; Shabat, D.; Satchi-Fainaro, R. Chemiluminescent probes in cancer biology. *Nat. Rev. Bioeng.* **2023**, *1*, 648–664, DOI: 10.1038/s44222-023-00074-0.

[14] Ran, C.; Pu, K. Molecularly Generated Light and its Biomedical Applications. *Angew. Chem. Int. Ed.* **2024**, *63*, e202314468, DOI: 10.1002/anie.202314468.

[15] M. Kaskova, Z.; S. Tsarkova, A.; V. Yampolsky, I. 1001 Lights: Luciferins, Luciferases, their Mechanisms of Action and Applications in Chemical Analysis, Biology and Medicine. *Chem. Soc. Rev.* **2016**, *45*, 6048–6077, DOI: 10.1039/C6CS00296J.

[16] Hananya, N.; Shabat, D. Recent Advances and Challenges in Luminescent Imaging: Bright Outlook for Chemiluminescence of Dioxetanes in Water. *ACS Cent. Sci.* **2019**,

5, 949–959, DOI: 10.1021/acscentsci.9b00372.

[17] Schaap, A. P.; Gagnon, S. D. Chemiluminescence from a Phenoxide-Substituted 1,2-dioxetane: a Model for Firefly Bioluminescence. *J. Am. Chem. Soc.* **1982**, *104*, 3504–3506, DOI: 10.1021/ja00376a044.

[18] Schaap, A. P.; Handley, R. S.; Giri, B. P. Chemical and enzymatic triggering of 1,2-dioxetanes. 1: Aryl esterase-catalyzed chemiluminescence from a naphthyl acetate-substituted dioxetane. *Tetrahedron Lett.* **1987**, *28*, 935–938, DOI: 10.1016/S0040-4039(00)95878-7.

[19] Schaap, A. P.; Chen, T.-S.; Handley, R. S.; DeSilva, R.; Giri, B. P. Chemical and enzymatic triggering of 1,2-dioxetanes. 2: fluoride-induced chemiluminescence from *tert*-butyldimethylsilyloxy-substituted dioxetanes. *Tetrahedron Lett.* **1987**, *28*, 1155–1158, DOI: 10.1016/S0040-4039(00)95313-9.

[20] Schaap, A. P.; Sandison, M. D.; Handley, R. S. Chemical and enzymatic triggering of 1,2-dioxetanes. 3: alkaline phosphatase-catalyzed chemiluminescence from an aryl phosphate-substituted dioxetane. *Tetrahedron Lett.* **1987**, *28*, 1159–1162, DOI: 10.1016/S0040-4039(00)95314-0.

[21] Haris, U.; Lippert, A. R. Exploring the Structural Space of Chemiluminescent 1,2-Dioxetanes. *ACS Sens.* **2023**, *8*, 3–11, DOI: 10.1021/acssensors.2c02371.

[22] Heffern, M. C.; Park, H. M.; Au-Yeung, H. Y.; Van de Bittner, G. C.; Ackerman, C. M.; Stahl, A.; Chang, C. J. In vivo Bioluminescence Imaging Reveals Copper Deficiency in a Murine Model of Nonalcoholic Fatty Liver Disease. *Proc. Natl. Acad. Sci. U.S.A.* **2016**, *113*, 14219–14224, DOI: 10.1073/pnas.1613628113.

[23] Cao, J.; Campbell, J.; Liu, L.; Mason, R. P.; Lippert, A. R. In Vivo Chemiluminescent Imaging Agents for Nitroreductase and Tissue Oxygenation. *Anal. Chem.* **2016**, *88*, 4995–5002, DOI: 10.1021/acs.analchem.6b01096.

[24] Cao, J.; Lopez, R.; Thacker, J. M.; Moon, J. Y.; Jiang, C.; Morris, S. N. S.; Bauer, J. H.; Tao, P.; Mason, R. P.; Lippert, A. R. Chemiluminescent Probes for Imaging H2S in Living Animals. *Chem. Sci.* **2015**, *6*, 1979–1985, DOI: 10.1039/C4SC03516J.

[25] Herbert, J. M.; Mandal, A. *Time-Dependent Density Functional Theory*; Jenny Stanford Publishing, 2022; p 44.

[26] Shao, Y.; Head-Gordon, M.; Krylov, A. I. The spin–flip approach within time-dependent density functional theory: Theory and applications to diradicals. *J. Chem. Phys.* **2003**, *118*, 4807–4818, DOI: 10.1063/1.1545679.

[27] Lee, S.; Filatov, M.; Lee, S.; Choi, C. H. Eliminating spin-contamination of spin-flip time dependent density functional theory within linear response formalism by the use of zeroth-order mixed-reference (MR) reduced density matrix. *J. Chem. Phys.* **2018**, *149*, 104101, DOI: 10.1063/1.5044202.

[28] Knieling, F.; Lee, S.; Ntziachristos, V. A primer on current status and future opportunities of clinical optoacoustic imaging. *npj Imaging* **2025**, *3*, 4, DOI: 10.1038/s44303-024-00065-9.

[29] Taruttis, A.; Ntziachristos, V. Advances in real-time multispectral optoacoustic imaging and its applications. *Nat. Photon* **2015**, *9*, 219–274, DOI: 10.1038/nphoton.2015.29.

[30] Ilina, K.; MacCuaig, W. M.; Laramie, M.; Jeouty, J. N.; McNally, L. R.; Henary, M. Squaraine Dyes: Molecular Design for Different Applications and Remaining Challenges. *Bioconjugate Chem.* **2020**, *31*, 194–213, DOI: 10.1021/acs.bioconjchem.9b00482.

[31] Lima, E.; Reis, L. V. 'Lights, Squaraines, Action!' – The Role of Squaraine Dyes in Photodynamic Therapy. *Future Med. Chem.* **2022**, *14*, 1375–1402, DOI: 10.4155/fmc-2022-0112.

[32] Adamo, C.; Barone, V. Toward Reliable Density Functional Methods without Adjustable Parameters: The PBE0 Model. *J. Chem. Phys.* **1999**, *110*, 6158–6170, DOI:

10.1063/1.478522.

[33] Perdew, J. P.; Burke, K.; Ernzerhof, M. Generalized Gradient Approximation Made Simple. *Phys. Rev. Lett.* **1996**, *77*, 3865–3868, DOI: 10.1103/PhysRevLett.77.3865.

[34] Hehre, W. J.; Ditchfield, R.; Pople, J. A. Self—Consistent Molecular Orbital Methods. XII. Further Extensions of Gaussian—Type Basis Sets for Use in Molecular Orbital Studies of Organic Molecules. *J. Chem. Phys.* **1972**, *56*, 2257–2261, DOI: 10.1063/1.1677527.

[35] Epifanovsky, E. et al. Software for the frontiers of quantum chemistry: An overview of developments in the Q-Chem 5 package. *J. Chem. Phys.* **2021**, *155*, 084801, DOI: 10.1063/5.0055522.

[36] Peach, M. J. G.; Sueur, C. R. L.; Ruud, K.; Guillaume, M.; Tozer, D. J. TDDFT diagnostic testing and functional assessment for triazene chromophores. *Phys. Chem. Chem. Phys.* **2009**, *11*, 4465–4470, DOI: 10.1039/B822941D.

[37] Preat, J.; Michaux, C.; Lewalle, A.; Perpète, E. A.; Jacquemin, D. Delocalisation in conjugated triazene chromophores: Insights from theory. *Chem. Phys. Lett.* **2008**, *451*, 37–42, DOI: 10.1016/j.cplett.2007.11.056.

[38] Wickizer, C.; Lander, C.; Pei, Z.; Yip, W. T.; Ran, C.; Shao, Y. A Computational Modeling of ADLumin Chemiluminescence: Oxygenation and Dioxetanone Formation. *J. Comput. Chem.* **2026**, *47*, e70372, DOI: 10.1002/jcc.70372.

[39] Hong, G.; Antaris, A. L.; Dai, H. Near-Infrared Fluorophores for Biomedical Imaging. *Nat. Biomed. Eng.* **2017**, *1*, 1–22, DOI: 10.1038/s41551-016-0010.

[40] Ran, C.; Mansfield, J. R.; Bai, M.; Viola, N. T.; Mahajan, A.; Delikatny, E. J. Practical Guidance for Developing Small-Molecule Optical Probes for In Vivo Imaging. *Mol. Imaging Biol.* **2023**, *25*, 240–264, DOI: 10.1007/s11307-023-01800-1.

[41] Miao, Q.; Xie, C.; Zhen, X.; Lyu, Y.; Duan, H.; Liu, X.; Jokerst, J. V.; Pu, K. Molecular Afterglow Imaging with Bright, Biodegradable Polymer Nanoparticles. *Nat. Biotechnol.* **2017**, *35*, 1102–1110, DOI: 10.1038/nbt.3987.

[42] Prescher, J. A.; Contag, C. H. Guided by the Light: Visualizing Biomolecular Processes in Living Animals with Bioluminescence. *Curr. Opin. Chem. Biol.* **2010**, *14*, 80–89, DOI: 10.1016/j.cbpa.2009.11.001.

[43] Van de Bittner, G. C.; Bertozzi, C. R.; Chang, C. J. Strategy for Dual-Analyte Luciferin Imaging: In Vivo Bioluminescence Detection of Hydrogen Peroxide and Caspase Activity in a Murine Model of Acute Inflammation. *J. Am. Chem. Soc.* **2013**, *135*, 1783–1795, DOI: 10.1021/ja309078t.

[44] Van de Bittner, G. C.; Dubikovskaya, E. A.; Bertozzi, C. R.; Chang, C. J. In vivo Imaging of Hydrogen Peroxide Production in a Murine Tumor Model with a Chemoselective Bioluminescent Reporter. *Proc. Natl. Acad. Sci. U.S.A.* **2010**, *107*, 21316–21321, DOI: 10.1073/pnas.1012864107.

[45] Branchini, B. R.; Ablamsky, D. M.; Davis, A. L.; Southworth, T. L.; Butler, B.; Fan, F.; Jathoul, A. P.; Pule, M. A. Red-Emitting Luciferases for Bioluminescence Reporter and Imaging Applications. *Anal. Biochem.* **2010**, *396*, 290–297, DOI: 10.1016/j.ab.2009.09.009.

[46] Branchini, B. R.; Southworth, T. L.; Fontaine, D. M.; Kohrt, D.; Talukder, M.; Michelini, E.; Cevenini, L.; Roda, A.; Grossel, M. J. An Enhanced Chimeric Firefly Luciferase-Inspired Enzyme for ATP Detection and Bioluminescence Reporter and Imaging Applications. *Anal. Biochem.* **2015**, *484*, 148–153, DOI: 10.1016/j.ab.2015.05.020.

[47] Rai, H.; Gupta, S.; Kumar, S.; Yang, J.; Singh, S. K.; Ran, C.; Modi, G. Near-Infrared Fluorescent Probes as Imaging and Theranostic Modalities for Amyloid-Beta and Tau Aggregates in Alzheimer's Disease. *J. Med. Chem.* **2022**, *65*, 8550–8595, DOI:

10.1021/acs.jmedchem.1c01619.

[48] Yeh, H.-W.; Ai, H.-W. Development and Applications of Bioluminescent and Chemiluminescent Reporters and Biosensors. *Annu. Rev. Anal. Chem.* **2019**, *12*, 129–150, DOI: 10.1146/annurev-anchem-061318-115027.

[49] Yao, Z.; Zhang, B. S.; Prescher, J. A. Advances in Bioluminescence Imaging: New Probes from Old Recipes. *Curr. Opin. Chem. Biol.* **2018**, *45*, 148–156, DOI: 10.1016/j.cbpa.2018.05.009.

[50] Paley, M. A.; Prescher, J. A. Bioluminescence: a Versatile Technique for Imaging Cellular and Molecular Features. *Med. Chem. Commun.* **2014**, *5*, 255–267, DOI: 10.1039/C3MD00288H.

[51] Yang, M.; Huang, J.; Fan, J.; Du, J.; Pu, K.; Peng, X. Chemiluminescence for Bioimaging and Therapeutics: Recent Advances and Challenges. *Chem. Soc. Rev.* **2020**, *49*, 6800–6815, DOI: 10.1039/D0CS00348D.

[52] Yang, J.; Zhu, B.; Zhang, J.; Liang, S. H.; Shen, S.; Ran, C. Half-Curcumin-Based Chemiluminescence Probes and Their Applications in Detecting Quasi-Stable Oxidized Proteins. *Angew. Chem. Int. Ed.* **2024**, *136*, e202409896, DOI: 10.1002/ange.202409896.

[53] Cao, J.; An, W.; Reeves, A. G.; Lippert, A. R. A Chemiluminescent Probe for Cellular Peroxynitrite using a Self-Immolative Oxidative Decarbonylation Reaction. *Chem. Sci.* **2018**, *9*, 2552–2558, DOI: 10.1039/C7SC05087A.

[54] Huang, J.; Huang, J.; Cheng, P.; Jiang, Y.; Pu, K. Near-Infrared Chemiluminescent Reporters for In Vivo Imaging of Reactive Oxygen and Nitrogen Species in Kidneys. *Adv. Funct. Mater.* **2020**, *30*, 2003628, DOI: 10.1002/adfm.202003628.

[55] Kondo, H.; Igarashi, T.; Maki, S.; Niwa, H.; Ikeda, H.; Hirano, T. Substituent Effects

on the Kinetics for the Chemiluminescence Reaction of 6-arylimidazo[1,2-*a*]pyrazin-3(7*H*)-ones (*Cypridina* luciferin Analogues): Support for the Single Electron Transfer (SET)–Oxygenation Mechanism with Triplet Molecular Oxygen. *Tetrahedron Lett.* **2005**, *46*, 7701–7704, DOI: 10.1016/j.tetlet.2005.09.014.

[56] Shimomura, O.; Johnson, F. H. Mechanism of the Luminescent Oxidation of Cypridina Luciferin. *Biochem. Biophys. Res. Commun.* **1971**, *44*, 340–346, DOI: 10.1016/0006-291X(71)90605-X.

[57] Fujimori, K.; Nakajima, H.; Akutsu, K.; Mitani, M.; Sawada, H.; Nakayama, M. Chemiluminescence of Cypridina luciferin analogues. Part 1. Effect of pH on Rates of Spontaneous Autoxidation of CLA in Aqueous Buffer Solutions. *J. Chem. Soc., Perkin Trans. 2* **1993**, 2405–2409, DOI: 10.1039/P29930002405.

[58] Teranishi, K. Luminescence of Imidazo[1,2-*a*]pyrazin-3(7*H*)-one Compounds. *Bioorg. Chem.* **2007**, *35*, 82–111, DOI: 10.1016/j.bioorg.2006.08.003.

[59] Magalhães, C. M.; Esteves da Silva, J. C. G.; Pinto da Silva, L. Comparative Study of the Chemiluminescence of Coelenterazine, Coelenterazine-e and *Cypridina* luciferin with an Experimental and Theoretical Approach. *J. Photochem. Photobiol. B* **2019**, *190*, 21–31, DOI: 10.1016/j.jphotobiol.2018.11.006.

[60] Branchini, B. R.; Behney, C. E.; Southworth, T. L.; Fontaine, D. M.; Gulick, A. M.; Vinyard, D. J.; Brudvig, G. W. Experimental Support for a Single Electron-Transfer Oxidation Mechanism in Firefly Bioluminescence. *J. Am. Chem. Soc.* **2015**, *137*, 7592–7595, DOI: 10.1021/jacs.5b03820.

[61] Chen, S.-F.; Navizet, I.; Roca-Sanjuán, D.; Lindh, R.; Liu, Y.-J.; Ferré, N. Chemiluminescence of Coelenterazine and Fluorescence of Coelenteramide: A Systematic Theoretical Study. *J. Chem. Theory Comput.* **2012**, *8*, 2796–2807, DOI: 10.1021/ct300356j.

[62] Ding, B.-W.; Naumov, P.; Liu, Y.-J. Mechanistic Insight into Marine Bioluminescence:

Photochemistry of the Chemiexcited Cypridina (Sea Firefly) Lumophore. *J. Chem. Theory Comput.* **2015**, *11*, 591–599, DOI: 10.1021/ct5009203.

[63] Pinto da Silva, L.; Magalhães, C. M.; Esteves da Silva, J. C. G. Interstate Crossing-Induced Chemiexcitation Mechanism as the Basis for Imidazopyrazinone Bioluminescence. *ChemistrySelect* **2016**, *1*, 3343–3356, DOI: 10.1002/slct.201600688.

[64] Pinto da Silva, L.; Pereira, R. F. J.; Magalhães, C. M.; Esteves da Silva, J. C. G. Mechanistic Insight into Cypridina Bioluminescence with a Combined Experimental and Theoretical Chemiluminescent Approach. *J. Phys. Chem. B* **2017**, *121*, 7862–7871, DOI: 10.1021/acs.jpcb.7b06295.

[65] Min, C.-G.; Liu, Q.-B.; Leng, Y.; Magalhães, C. M.; Huang, S.-J.; Liu, C.-X.; Yang, X.-K.; Da Silva, L. P. Mechanistic Insight into the Chemiluminescent Decomposition of *Cypridina* Dioxetanone and the Chemiluminescent, Fluorescent Properties of the Light Emitter of *Cypridina* Bioluminescence. *J. Chem. Inf. Model.* **2019**, *59*, 4393–4401, DOI: 10.1021/acs.jcim.9b00614.

[66] Liu, F.; Liu, Y.; De Vico, L.; Lindh, R. Theoretical Study of the Chemiluminescent Decomposition of Dioxetanone. *J. Am. Chem. Soc.* **2009**, *131*, 6181–6188, DOI: 10.1021/ja808511t.

[67] Yue, L.; Lan, Z.; Liu, Y.-J. The Theoretical Estimation of the Bioluminescent Efficiency of the Firefly via a Nonadiabatic Molecular Dynamics Simulation. *J. Phys. Chem. Lett.* **2015**, *6*, 540–548, DOI: 10.1021/jz502305g.

[68] Xie, J.-M.; Leng, Y.; Cui, X.-Y.; Min, C.-G.; Ren, A.-M.; Liu, G.; Yin, Q. Theoretical Study on the Formation and Decomposition Mechanisms of Coelenterazine Dioxetanone. *J. Phys. Chem. A* **2023**, *127*, 3804–3813, DOI: 10.1021/acs.jpca.3c00453.

[69] Isobe, H.; Takano, Y.; Okumura, M.; Kuramitsu, S.; Yamaguchi, K. Mechanistic

Insights in Charge-Transfer-Induced Luminescence of 1,2-Dioxetanones with a Substituent of Low Oxidation Potential. *J. Am. Chem. Soc.* **2005**, *127*, 8667–8679, DOI: 10.1021/ja043295f.

[70] Gerbig, D.; Schreiner, P. R. Preparation and Spectroscopic Identification of the Cyclic CO_2 Dimer 1,2-Dioxetanedione. *J. Am. Chem. Soc.* **2023**, *145*, 22341–22346, DOI: 10.1021/jacs.3c08894.

[71] McCapra, F.; Chang, Y. C. The Chemiluminescence of a Cypridina luciferin Analogue. *Chem. Commun. (London)* **1967**, 1011–1012, DOI: 10.1039/C19670001011.

[72] McCapra, F. Chemical Mechanisms in Bioluminescence. *Acc. Chem. Res.* **1976**, *9*, 201–208, DOI: 10.1021/ar50102a001.

[73] Isobe, M.; Takahashi, H.; Usami, K.; Hattori, M.; Nishigohri, Y. Bioluminescence Mechanism on New Systems. *Pure Appl. Chem.* **1994**, *66*, 765–772, DOI: 10.1351/pac199466040765.

[74] Goto, T. Chemistry of Bioluminescence. *Pure Appl. Chem.* **1968**, *17*, DOI: 10.1351/pac196817030421.

[75] Isobe, H.; Yamanaka, S.; Kuramitsu, S.; Yamaguchi, K. Regulation Mechanism of Spin-Orbit Coupling in Charge-Transfer-Induced Luminescence of Imidazopyrazinone Derivatives. *J. Am. Chem. Soc.* **2008**, *130*, 132–149, DOI: 10.1021/ja073834r.

[76] Wu, N.; Xu, Z.-C.; Du, K.-D.; Huang, S.; Kobayashi, N.; Kuroda, Y.; Bai, Y.-H. A Structural Model of Truncated Gaussia princeps Luciferase Elucidating the Crucial Catalytic Function of No.76 Arginine towards Coelenterazine Oxidation. *PLOS Comput. Biol.* **2025**, *21*, e1012722, DOI: 10.1371/journal.pcbi.1012722.

[77] Yeh, A. H.-W. et al. De novo Design of Luciferases using Deep Learning. *Nature* **2023**, *614*, 774–780, DOI: 10.1038/s41586-023-05696-3.

[78] Ding, B.-W.; Liu, Y.-J. Bioluminescence of Firefly Squid via Mechanism of Single Electron-Transfer Oxygenation and Charge-Transfer-Induced Luminescence. *J. Am. Chem. Soc.* **2017**, *139*, 1106–1119, DOI: 10.1021/jacs.6b09119.

[79] Epifanovsky, E. et al. Software for the Frontiers of Quantum Chemistry: An Overview of Developments in the Q-Chem 5 Package. *J. Chem. Phys.* **2021**, *155*, 084801, DOI: 10.1063/5.0055522.

[80] Marenich, A. V.; Cramer, C. J.; Truhlar, D. G. Universal Solvation Model Based on Solute Electron Density and on a Continuum Model of the Solvent Defined by the Bulk Dielectric Constant and Atomic Surface Tensions. *J. Phys. Chem. B* **2009**, *113*, 6378–6396, DOI: 10.1021/jp810292n.

[81] Harvey, J. N.; Aschi, M.; Schwarz, H.; Koch, W. The Singlet and Triplet States of Phenyl Cation. A Hybrid Approach for Locating Minimum Energy Crossing Points Between Non-interacting Potential Energy Surfaces. *Theor. Chem. Acc.* **1998**, *99*, 95–99, DOI: 10.1007/s002140050309.

[82] Harvey, J. N. Spin-Forbidden Reactions: Computational Insight into Mechanisms and Kinetics. *WIREs Comput. Mol. Sci.* **2014**, *4*, 1–14, DOI: 10.1002/wcms.1154.

[83] Lu, T. sobMECP Program. `http://sobereva.com/286.`

[84] Pinto da Silva, L.; Esteves da Silva, J. C. G. Interstate Crossing-Induced Chemiexcitation as the Reason for the Chemiluminescence of Dioxetanones. *ChemPhysChem* **2013**, *14*, 1071–1079, DOI: 10.1002/cphc.201200872.

[85] Augusto, F. A.; Francés-Monerris, A.; Galván, I. F.; Roca-Sanjuán, D.; Bastos, E. L.; Baader, W. J.; Lindh, R. Mechanism of Activated Chemiluminescence of Cyclic Peroxides: 1,2-dioxetanes and 1,2-dioxetanones. *Phys. Chem. Chem. Phys.* **2017**, *19*, 3955–3962, DOI: 10.1039/C6CP08154A.

[86] Silva, L. P. d.; Magalhães, C. M.; Crista, D. M. A.; Silva, J. C. G. E. d. Theoretical Modulation of Singlet/Triplet Chemiexcitation of Chemiluminescent Imidazopyrazinone Dioxetanone via C8-Substitution. *Photochem. Photobiol. Sci.* **2017**, *16*, 897–907, DOI: 10.1039/C7PP00012J.

[87] Koo, J.; Schmidt, S.; Schuster, G. Bioluminescence of the firefly: key steps in the formation of the electronically excited state for model systems. *Proc. Natl. Acad. Sci.* **1978**, *75*, 30–33, DOI: 10.1073/pnas.75.1.30.

[88] Schmidt, S. P.; Schuster, G. B. Dioxetanone chemiluminescence by the chemically initiated electron exchange pathway. Efficient generation of excited singlet states. *J. Am. Chem. Soc.* **1978**, *100*, 1966–1968, DOI: 10.1021/ja00474a074.

[89] Hirano, T.; Takahashi, Y.; Kondo, H.; Maki, S.; Kojima, S.; Ikeda, H.; Niwa, H. The reaction mechanism for the high quantum yield of Cypridina (Vargula) bioluminescence supported by the chemiluminescence of 6-aryl-2-methylimidazo[1,2-a]pyrazin-3(7H)-ones (Cypridina luciferin analogues). *Photochem. Photobiol. Sci.* **2008**, *7*, 197–207, DOI: 10.1039/B713374J.

[90] Watanabe, N.; Kikuchi, M.; Maniwa, Y.; Ijuin, H. K.; Matsumoto, M. Synthesis of Sulfanyl-, Sulfinyl-, and Sulfonyl-Substituted Bicyclic Dioxetanes and Their Base-Induced Chemiluminescence. *J. Org. Chem.* **2010**, *75*, 879–884, DOI: 10.1021/jo902477n.

[91] Tanimura, M.; Watanabe, N.; Ijuin, H. K.; Matsumoto, M. Thermodynamic Aspects of Thermal Decomposition and Charge-Transfer-Induced Chemiluminescent Decomposition for Bicyclic Dioxetanes Bearing a 4-(Benzothiazol-2-yl)-3-hydroxyphenyl Moiety. *J. Org. Chem.* **2010**, *75*, 3678–3684, DOI: 10.1021/jo100449m.

[92] Matsumoto, M.; Kakuno, F.; Kikkawa, A.; Hoshiya, N.; Watanabe, N.; Ijuin, H. K. Alkaline metal ion-enhanced chemiluminescence of bicyclic dioxetanes bearing a hydroxyaryl group with an '*even*' substitution pattern. *Tetrahedron Lett.* **2009**, *50*, 2337–2341, DOI: 10.1016/j.tetlet.2009.02.190.

[93] Grimme, S.; Ehrlich, S.; Goerigk, L. Effect of the damping function in dispersion corrected density functional theory. *J. Comput. Chem.* **2011**, *32*, 1456–1465, DOI: 10.1002/jcc.21759.

[94] Becke, A. D. A new mixing of Hartree–Fock and local density-functional theories. *J. Chem. Phys.* **1993**, *98*, 1372–1377, DOI: 10.1063/1.464304.

[95] Behn, A.; Zimmerman, P. M.; Bell, A. T.; Head-Gordon, M. Efficient exploration of reaction paths via a freezing string method. *J. Chem. Phys.* **2011**, *135*, 224108, DOI: 10.1063/1.3664901.

[96] Barone, V.; Cossi, M. Quantum Calculation of Molecular Energies and Energy Gradients in Solution by a Conductor Solvent Model. *J. Phys. Chem. A* **1998**, *102*, 1995–2001, DOI: 10.1021/jp9716997.

[97] Chai, J.-D.; Head-Gordon, M. Long-range corrected hybrid density functionals with damped atom–atom dispersion corrections. *Phys. Chem. Chem. Phys.* **2008**, *10*, 6615–6620, DOI: 10.1039/B810189B.

A

Appendix

Supplemental information

A.1 Supplemental information for Chapter 2

Table A.1: Wavelengths (in nm) and oscillator strengths (in au) for the lowest energy absorption, as well as vibrational entropies (in cal/mol/K) of squaraine analogs calculated using the PBE functional and 6-31+G* basis set.

X	R	λ_{01} (nm)	f_{01} (au)	S_{vib} (cal/mol/K)
Br	ETM	701.6	0.103	197.3
Cl	ETM	704.0	0.080	194.2
F	ETM	698.9	0.060	190.9
H	ETM	700.8	0.051	183.6
Br	CH_3	752.3	0.002	129.8
H	CH_3	741.5	0.002	115.1

A.2 Supplemental information for Chapter 3

A.2.1 Conformations of ADLumin molecules

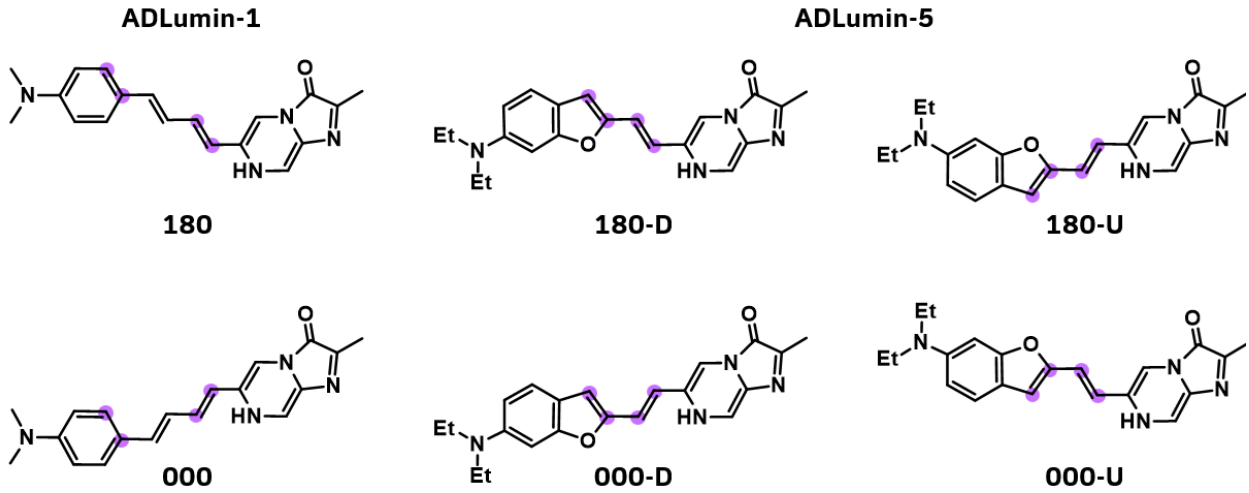

Figure A.1: Conformations of ADLumin-1 and ADLumin-5. 000 and 180 indicate the torsional angle of the atoms circled in purple. For ADLumin-5, -D and -U indicate down and up positions of the benzofuran oxygen atom

Table A.2: Energies (in kcal/mol) of 000-D, 000-U, 180-D, and 180-U ADLumin reactant conformations from unrestricted DFT calculations using the PBE0 functional, 6-31+G* basis set, and SMD model for water. The naming convention is demonstrated in Fig. A.1.

Conformation	ADLumin-5	ADLumin-6	ADLumin-7	ADLumin-8
000-D	2.45	2.46	1.64	1.69
000-U	3.99	3.96	4.01	3.99
180-D	2.37	2.19	1.76	1.74
180-U	0.00	0.00	0.00	0.00

Table A.3: Energies (in kcal/mol) of 000 and 180 ADLumin-1 reactant conformations from unrestricted DFT calculations using the PBE0 functional, 6-31+G* basis set, and SMD model for water. The naming convention is demonstrated in Fig. A.1.

Conformation	ADLumin-1
000	0.00
180	1.61

A.2.2 Oxygenation of ADLumin-5

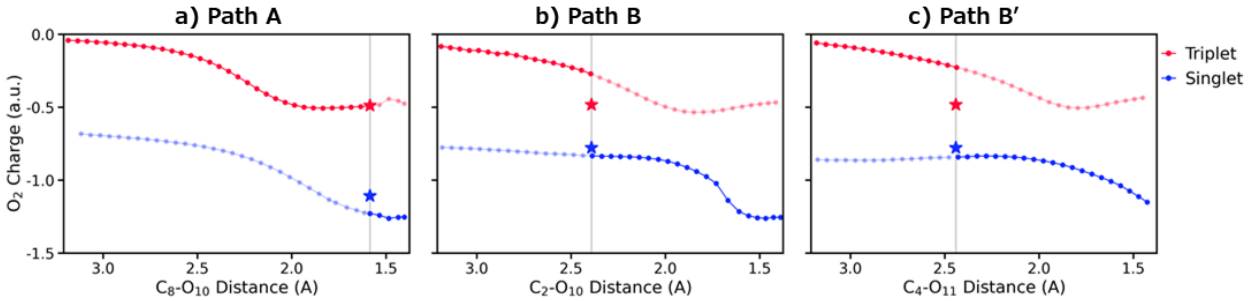

Figure A.2: ChElPG charges for O_2 calculated along the singlet and triplet minimum energy paths for the formation of intermediate 1. a) Path A, b) Path B, and c) Path B'. Unrestricted DFT calculations were performed using the PBE0 functional, 6-31+G* basis set, and SMD model for water.

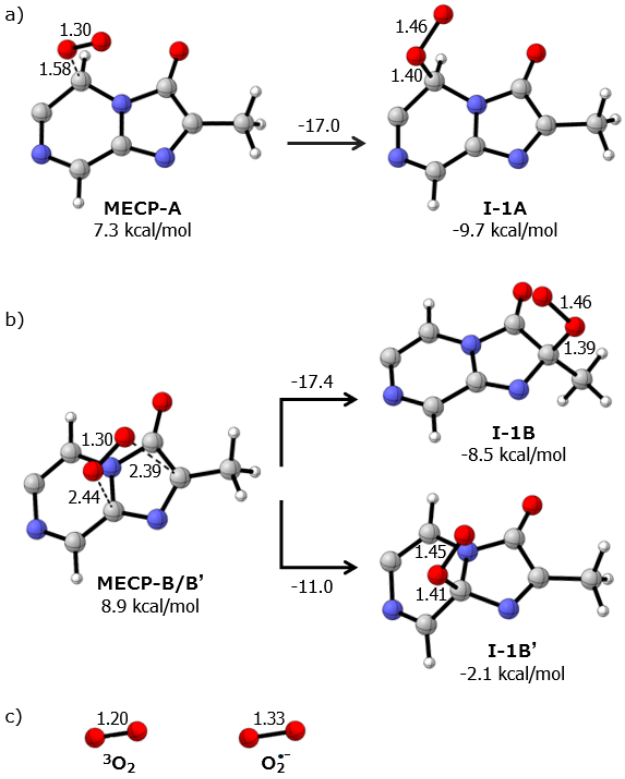

Figure A.3: MECP and I-1 structures, bond distances, and energies for a) Path A, and b) Paths B and B'. c) Bond distances for O_2 calculated as a triplet and a doublet superoxide anion radical. Unrestricted DFT calculations were performed using the PBE0 functional, 6-31+G* basis set, and SMD model for water.

A.2.3 Reaction paths for ADLumin-X molecules

Table A.4: Minimum Energy Crossing Point (MECP), Intermediate (I), and Transition State (TS) energies (in kcal/mol) of ADLumin-X molecules from unrestricted DFT calculations using the PBE0 functional, 6-31+G* basis set, and SMD model for water. All energies are plotted relative to reactants ($^3O_2$ and singlet ADLumin-X).

	ADLumin-5	ADLumin-6	ADLumin-7	ADLumin-8
MECP-A	7.36	3.30	7.75	7.75
I-2A	-5.26	-9.67	-4.46	-4.44
TS-2A	10.80	11.97	11.58	11.62
I-3A	-10.97	-9.27	-10.31	-10.36
MECP-B/B'	8.94	11.70	9.06	9.07
I-1B'	-2.11	0.47	-2.08	-2.09
TS-1B'	6.37	8.16	6.29	6.28
I-2B'	6.20	7.84	6.09	6.11
I-2B	-10.38	-9.37	-10.48	-10.49
TS-2B	-5.21	-6.75	-5.42	-5.44
I-3B	-8.38	-11.15	-8.52	-8.54

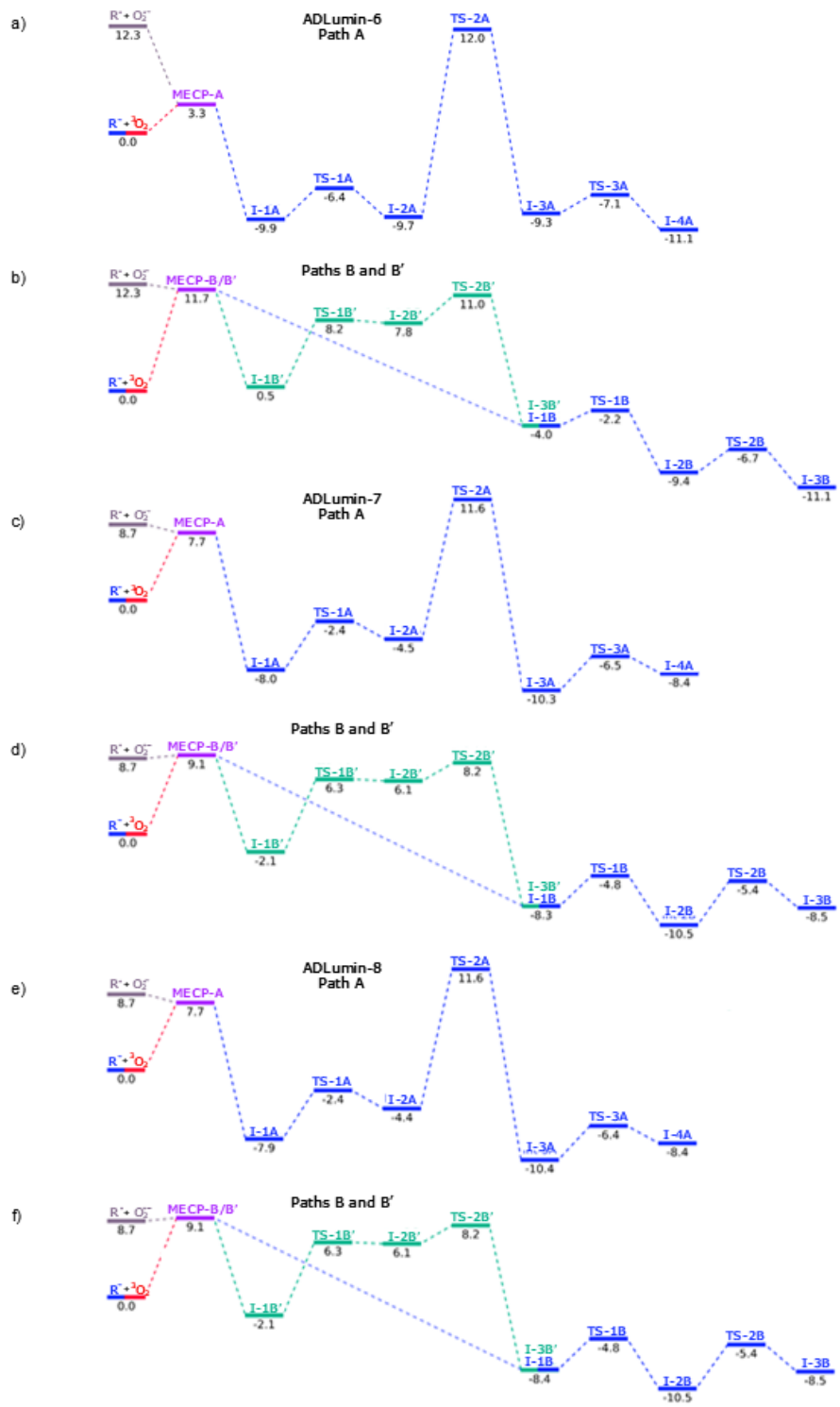

Figure A.4: Paths A, B, and B' for ADLumin-6 (a-b), ADLumin-7 (c-d). and ADLumin-8 (e-f). Unrestricted DFT calculations were performed using PBE0 functional, 6-31+G* basis set, and SMD model for water.

A.3 Supplemental information for Chapter 4

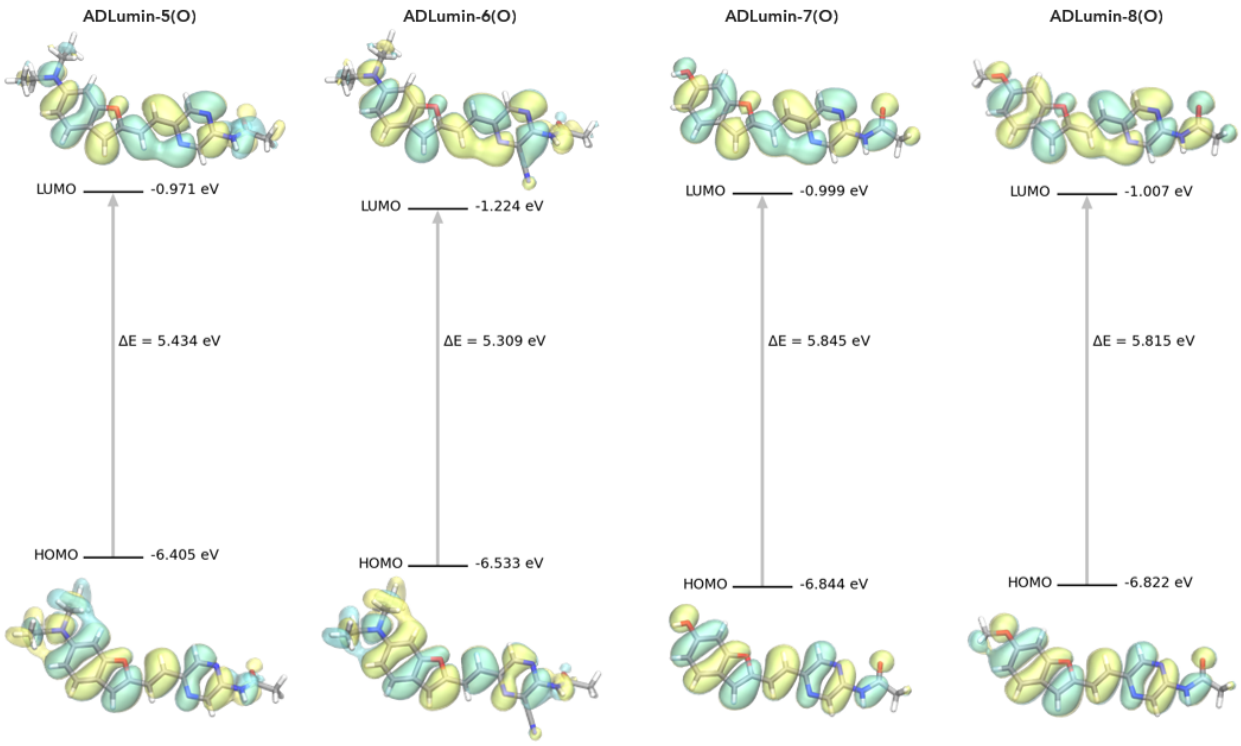

Figure A.5: HOMO-LUMO gaps for the neutral ADLumin-X open ring products. DFT calculations were performed using the ωB97X-D functional, 6-31+G* basis set, and PCM model for DMSO. Adapted from ref 4.